SANDIA REPORT

SAND2004-4962
Unlimited Release
Printed October 2004

Molecular Dynamics of Membrane Proteins

Mark J. Stevens, Paul Crozier and Thomas Woolf

Sandia National Laboratories

Molecular Dynamics of Membrane Proteins

Mark Stevens
Computational Materials and Molecular Sciences

Paul Crozier
Computational Materials and Molecular Biology

Sandia National Laboratories
P.O. Box 5800
Albuquerque, NM 87185-1411

Thomas Woolf
Department of Physiology
Johns Hopkins University School of Medicine
725 N. Wolfe St.
Baltimore, MD 21205

Abstract

Understanding the dynamics of the membrane protein rhodopsin will have broad implications for other membrane proteins and cellular signaling processes. Rhodopsin (Rho) is a light activated G-protein coupled receptor (GPCR). When activated by ligands, GPCRs bind and activate G-proteins residing within the cell and begin a signaling cascade that results in the cell's response to external stimuli. More than 50% of all current drugs are targeted toward G-proteins. Rho is the prototypical member of the class A GPCR superfamily. Understanding the activation of Rho and its interaction with its G-protein can therefore lead to a wider understanding of the mechanisms of GPCR activation and G-protein activation. Understanding the dark to light transition of Rho is fully analogous to the general ligand binding and activation problem for GPCRs. This transition is dependent on the lipid environment. The effect of lipids on membrane protein activity in general has had little attention, but evidence is beginning to show a significant role for lipids in membrane protein activity. Using the LAMMPS program and simulation methods benchmarked under the IBIG program, we perform a variety of all-atom molecular dynamics simulations of membrane proteins.

Contents

CHAPTER 4 ATOMISTIC SIMULATIONS OF BIOLOGICALLY REALISTIC TRANSMEMBRANE POTENTIAL GRADIENTS 40

Chapter 1 Introduction

Understanding the dynamics of the membrane protein rhodopsin will have broad implications for other membrane proteins and cellular signaling processes. Rhodopsin is a light activated G-protein coupled receptor (GPCR). G-proteins reside within the cell and begin the signaling cascade that results in the cell's response to external stimuli (Figure 1). More than 50% of all current drugs are targeted toward G-proteins. Since rhodopsin is a prototypical member of the class A GPCR superfamily, there is the opportunity for rational under-standing of receptor activation and coupling by understanding the interaction of rhodopsin with its G-pro-tein. The crystal structure is known only for the dark-adapted state, and our
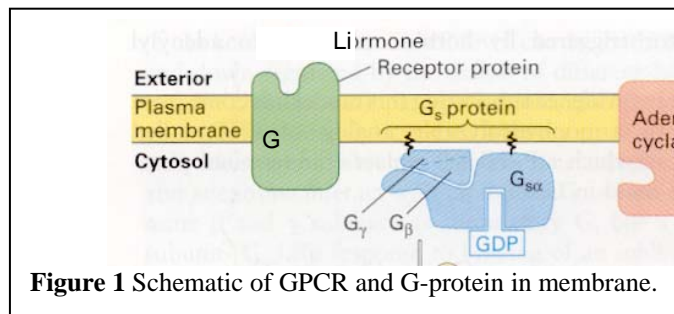
Figure 1 Schematic of GPCR and G-protein in membrane.

simulations to date have been performed for this state. Understanding the dark to light transition is a fundamental issue for rhodopsin and is related to general ligand binding of GPCRs. This transition is dependent on the lipid environment. The effect of lipids on membrane protein activity in general has had little attention, but evidence is beginning to show a significant role for lipids in membrane protein activity. The coupling of rhodopsin to its G-protein is not understood. Thus, for more than one reason, understanding rhodopsin is key to gaining a better understanding of membrane proteins in general. Rhodopsin is one of the few membrane proteins for which there is a crystal structure, which makes molecular dynamics simulations possible. We will perform molecular dynamics simulations to investigate the above issues. Specifically, we will examine the coupling of conformational changes in the protein during the process of activation, and corresponding changes in the chemical environment of different residues in the protein.

Technical Approach and Expected Results

We laid the foundation for our work by per-forming initial molecular dynamics (MD) simu-lations of rhodopsin under the IBIG grand chal-lenge LDRD. The LAMMPS code has been modi-fied in order to make it compatible with molecular simulation methods and protocols widely accepted in the computational biology community. The LAMMPS MD code and subsidiary setup codes have enabled us to perform a 40 ns simulation of dark-adapted rhodopsin as well as 20 ns simulations of bacteriorhodopsin in the dark and intermediate states. These atomistic simulations include the rhodopsin protein in a lipid bilayer surrounded by water (Figure 2). This represents state-of-the-art simulation capability.

As described above, rhodopsin is a key membrane protein for many reasons. A major part
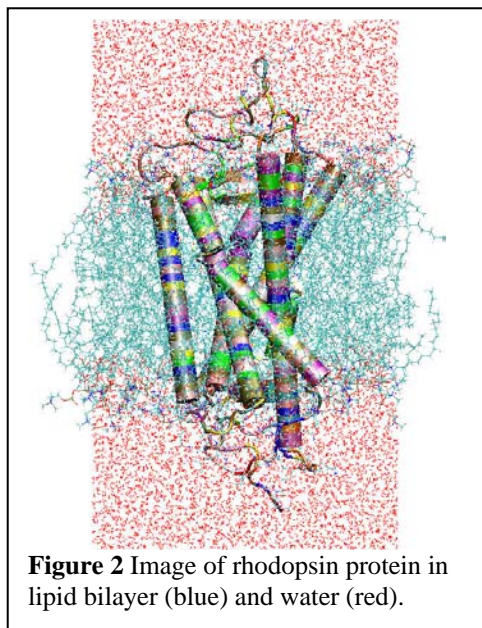
Figure 2 Image of rhodopsin protein in lipid bilayer (blue) and water (red).

of the work in this project is the simulation of rhodopsin after isomerization has occurred. We completed a 150 ns simulation which is remarkable feat. Our initial analysis of this work is given in Chapter 2. In order to understand the nature of transmembrane helices in membrane proteins, we have analyzed simulations of single helices of rhodopsin and compare their structures to the corresponding intact helix.

Examine rhodopsin activation and the lipid coupling to protein motion.

The first core problem is the dynamics of rhodopsin, particularly the dark-to-light transition and the effect of the lipid bilayer on rhodopsin dynamics. Rhodopsin is a ligand receptor that has been adapted to function as a photoreceptor, and its dark-to-light transition is a prototype for the activation of GPCRs. An important characteristic of rhodopsin is the dependence of its activity on the type of lipid in the membrane. This shows that rhodopsin dynamics is not solely a function of the protein.

We performed biased molecular dynamics simulations with consideration of experimental constraints to elucidate details of the large scale conformational change that rhodopsin undergoes during light activation. This involves biasing the retinal dynamics so that it undergoes the *cis-trans* isomerization. The consequent large-scale structural changes has been analyzed by dynamic importance sampling. In this way, we can remove the bias from the dynamics and calculate the free energy difference between the two structures. In addition to the calculation of the free energy, we have performed a very long (150 ns) simulation of rhodopsin that is continues from our 40 ns simulation of rhodopsin in the dark state, but with the *cis-trans* isomerization having been BLAH

Single helix simulations

Even though membrane proteins are extremely important to cell function and make up 20-30% of the genome, few well-defined structures of membrane proteins have been published owing partly to the difficulty of membrane protein crystallization. The dark-adapted form of bovine rhodopsin is a notable exception and provides considerable insight into the structure and function of a large class of membrane proteins. The protein folding problem is especially difficult in the case of membrane proteins since the mechanism of assembly is not entirely clear and involves the membrane. It has been postulated that individual transmembrane helices form first, followed by formation of the native transmembrane helix bundle conformation. This presupposes that transmembrane helices are independently stable units of secondary structure, and raises the question: if isolated, do individual transmembrane helices maintain native conformation, or are their structures highly dependent on the remainder of the protein? We address this issue in Chapter 3.

Membranes with a potential gradient

One of the key aspect of membrane is control of the electrostatic potential. Ion channels control the ion concentration of a given type on both sides of the membrane. The potential gradient that results form these ion concentrations is a key aspect of membrane system. All-atom molecular dynamics simulations have been used

successfully to study details of interactions between ions and ion channels and between ions and bilayers. However, because of limitations in the time- and length-scales accessible to all-atom simulations, MD has not been used to explicitly model the transmembrane potential gradient. Biologically relevant potential gradients are on the order of 100 mV, corresponding to a small asymmetric build-up of ions in the interfacial regions of the two monolayer leaflets of a lipid bilayer (on the order of 1 excess ion/10^4 $\mathring{A}^2$ of bilayer). An all-atom representation of this ion:lipid ratio requires on the order of 10^5 atoms, historically too many. This limitation led to the development of implicit representations of both the transmembrane potential and the membrane itself, which have reduced number of atoms. A straightforward solution to the periodicity problem is to simulate more than one bilayer per unit cell, but until now this has been considered too computationally expensive. Here, we implement this approach, which allows for full three-dimensional periodicity and an all-atom representation of the transmembrane potential with no continuum approximations. This work is described in Chapter 4.

Chapter 2 Long time simulation of Rhodopsin with retinal in the *trans* state

We examine the effect of retinal isomerization in rhodopsin by all atom molecular dynamics simulation, which includes explicit membrane lipids and water. The isomerization is performed by constraining the C11-C12 dihedral angle to undergo the *cis* to *trans* transition during a short simulation. Subsequently, the constraint is turned off and we follow the free response of the system to the isomerization in a 150 ns simulation. The structural dynamics of the 150 ns trajectory and its energetics have been examined. In particular, the helix tilt and kink angles have been calculated. Certain helices show changes in the orientation beyond that present in equilibrium simulations of the dark-adapted state. During the first 70 ns after isomerization Helices 5 and 6 change their orientation. Thereafter, the orientation remains steady. At 70 ns a set of transition occurs. A sharp transition occurs in the Glu 113 interaction energy with retinal, because the salt bridge is broken. The connection between large scale helix motion and small scale residue side chain motion is discussed. Connection to experimental data is also discussed. For example, the ionone ring moves closer to Ala 169 as it must according to crosslinking experiments.

Introduction

Rhodopsin is the prototypical G-protein coupled receptor (GPCR) due to the large amount of experimental information related to both its structure and its function (for recent reviews, see (Sakmar, 2002; Shi 2002; Filipek, 2003; Burns 2001 and Hubbell, 2003). It is also the first GPCR with a defined tertiary structure and is thus an excellent candidate for trying to understand the molecular details of function. A full understanding of these details is difficult, however, due to the large separation in time-scales between the photocycle of rhodopsin and current computational limits in computer simulation of bio-molecules. In particular, the full photocycle occurs on the millisecond time scale (Klein 2002), while the state-of-the-art in computer simulation of large proteins is tens of nanoseconds.

Bovine rhodopsin has served as a model system for the understanding of transduction for many years. In particular, studies in bovine rods have led to a general understanding of G-protein coupled systems, and have led to the first GPCR that was sequenced (Ferretti, 1986), and to understanding of the connections between particular residues and the rhodopsin function. (Fung, 1980; Filipek, 2003) For example, the role of Glu 113 as the counterion (Sakmar, 1989), the critical role of certain residues in transduction (Franke, 1990; Rao, 1996), and initial suggestions for spectral tuning (Zhukovsky, 1989; Yokoyama, 2002; Kuwayam, 2002) all begin with rhodopsin.   An upcoming frontier is the understanding of the connections between the structures of the G-protein itself (Noel, 1993; Lambright, 1994) and the conformational changes that underlie the photocycle and lead to activation and signaling.

A key aspect of understanding rhodopsin and other GPCR is the dynamics of the ligand activation. In rhodopsin, the *cis-trans* photoisomerization of retinal is the activation mechanism. The structural and energetic consequences of retinal's

isomerization are of great interest. Molecular dynamics (MD) simulations offer a means to obtain atomic scale dynamics of such systems. A main limitation has been the short time scales attainable in all atom MD simulations. However, we have been able to perform a 150 ns simulation, which is sufficiently long to examine important dynamical events along the path from the dark adapted to the light adapted state. The transition to the LUMI intermediate state takes about 150 ns. Thus, we are within range of an early rhodopsin intermediate and can compare to corresponding experimental data. In the simulation, by constraining the C11-C12 dihedral angle of retinal, we force the isomerization. In the subsequent dynamics, the constraint is turned off. We obtain a single trajectory of the consequences of the isomerization on the structure and energetics of rhodopsin. Within this comparison, we recognize that the simulation yields only one pathway to the state at 150 ns, not the statistical ensemble that actually exists. Similarly, we have only one state at 150 ns, or, a subset of the states that exist within, for example, 10 ns of the 150 ns state. However, some aspects of the dynamics are highly probable and will occur for most trajectories. We expect to see such dynamics in our simulation.

The details of the simulations are given in the methods section. We then describe the results of the simulation analysis concerning the structural dynamics and the energetics.

Simulation method

Including the effects of the lipid environment on rhodopsin structure and motion is important. Thus, we built, from the start, a system to include all-hydrogen, all-atom representations of protein, lipid, and water (Crozier, 2003). For this, it was important to use a consistent force-field that balanced the energies between each of these types of molecules. We elected to work with the CHARMM all-hydrogen force field (version 22 for protein and version 27 for lipids, both released in August of 1999) (Shlenkrich, 1996; MacKerell, 1998) and used the parameters defined for retinal within the CHARMM force field (Nina, 1993). Furthermore, we designed a system that included at least two lipid molecules surrounding the protein in the planar *xy*-directions. Periodic images were used in the *z*-dimension to represent a multilayer system such as studied experimentally by NMR methods. The total system size (41,623 atoms) consisted of protein, 99 DOPC lipids, 100 milli-molar salt concentration (14 sodium, 16 chloride), palmitylated lipids attached to Cys 322 and 323, and 7441 TIP3 waters. All calculations started from the first X-ray structure of rhodopsin (1F88) (Palczewski, 2000). The CHARMM program was used for the initial construction of the starting point and for the relaxation of the system to a production-ready stage. A modified version of the LAMMPS (Plimpton, 1995) code using the CHARMM force field was verified to produce exactly the same energies as the CHARMM code for the initial conformation.

Structural dynamics

Figure 1 shows the dihedral angle of the C11-C12 dihedral in retinal as a function of time including both the 150 ns after isomerization and the 40 ns before the isomerization. The data shows that the transition is stable; the dihedral angle does not change during the 150 ns simulation run. Other parts of the retinal molecule do undergo structural changes after isomerization. For example, the CG-CD dihedral has back-and-forth transitions from dihedral angles of 180° and 60°. Retinal's self-energy rises by

about 7 kcal/mol after isomerization. This change is primarily due to the C11-C12 dihedral transition. At about 30 ns, the self-energy drops sharply to below the average *cis* state self-energy and subsequently slowly decreases to about 4 kcal/mol below the *cis* state self-energy. This drop in energy also is primarily due to dihedral interactions. Other dihedrals than the C11-C12 relax after isomerization resulting in a net lower self-energy.

Figure 2 shows a structural connection to experimental data. The distance between retinal's ionone ring and Ala 169 decreases after isomerization. The final distance appears to reach a steady state separation of 9Å. This is consistent with crosslinking experiments (Borhan, 2000) which find that Ala 169 and the ionone ring can be crosslinked for rhodopsin in the LUMI state. Ala 169, which is part of Helix 4, is on the far side of the helix with respect to retinal in the dark state of rhodopsin. It is inferred that Ala 169 moves to the retinal side of Helix 4. This implies that Helix 4 has rotated as part of the transition to the LUMI state. Our final configuration does not show that Helix 4 has rotated and that Ala 169 is on the retinal side. As such, the retinal molecule the separation between the ionone ring and Ala 169 is still too far for the crosslink to occur. However, if Helix 4 were to rotate, then the ionone ring is in position to allow a crosslink to Ala 169. As noted above, only a single simulation has been performed. One expects that there is a set of conformations for the Lumi state, and only a (unknown) fraction of them allow the ionone:Ala 169 crosslinking. Our simulation does show that the separation distance is reduced significantly, and if Helix 4 rotates, then crosslinking can occur.

The structural changes that occur in the rhodopsin protein can be characterized in many ways. Given that rhodopsin consists of 7 transmembrane helices, we examined the tilt and kink of each helix throughout the simulation run. For the tilt angles, we calculate the tilt of each part of the helix, where the parts have been defined in terms of the kink centers. See (Crozier, 2003) for details of the definitions.

Figure 3 shows the tilt angles as a function of time for Helices 5b, 5c, 6b and 7a. These tilt angles show significant motion during the run. At about $t = 32$ ns, the tilt angles for Helices 5b and 5c undergo a large change (greater than the short time scale fluctuations). For 5b, the tilt angle rises and continues to slowly rise until the end of the simulation. Part 5c reaches a steady state by about $t = 70$ ns and fluctuates about 30 degrees. This structural change in tilt angle is also reflected in the change in kink angle for 5b-5c (Fig. 4). There is a sudden drop in the kink angle at $t = 32$ ns. Ultimately, this kink angle changes from 25° in the dark adapted state to about 5° at $t = 150$ ns. This small kink angle reflects the fact that the tilt angles of 5b and 5c become almost identical after the transition. Thus, the main effect in the simulation is almost complete removal of the kink in Helix 5. The retinal ionone ring is close to Helix 5. It is not surprising that Helix 5 changes its orientation in response to the movement of the ionone ring, which isomerization causes.

Helix 7 part (a) contains Lys 296. It is not surprising that the tilt angle is quickly influenced by the retinal isomerization. Figure 6 shows that the tilt angle increases within the tilt angle fluctuation time scale. At about $t = 70$ ns, the tilt angle returns to the dark state value. Thus, here again we have a correlation with the set of dynamics occurring at $t = 70$ ns. Given that the dynamics involves retinal and sides chains that interact strongly with Lys 296 (e.g. Glu 113), the correlation is to be expected.

The tilt angle for Helix part 6b decreases from its dark state value of 35° to an average of about 17°. This transition takes about 70 ns to occur. This is another example of the need for such long simulations as we have performed. The kink angle between Helix 6a and 6b (Fig. 4) shows a correlated dynamics. The kink angle decreases for the same 70 ns and thereafter oscillates about an average value of 20°. In this case, it is the tilt angle of part b that is the major part of the dynamics. The kink angle change is a result of just 6b's tilt dynamics.

Retinal is bonded to Helix 7. Thus, the structural changes due to the isomerization of retinal directly result in forces on Helix 7. Immediately after isomerization, the tilt angle of Helix 7a increases from about 7° to 15°. At about $t = 70$ ns (where the changes in Helix 6 tilt angle stop), the tilt angle abruptly returns to the dark state value.

The local dihedral dynamics of two side chains is given in Fig. 6. The dihedral dynamics of Ser 186 even in the dark adapted state is not constant, as hydrogen bonds between Ser 186 and other residues are exchanged (Crozier, 2003). After isomerization, the dihedral angle of Ser 186 remains constant for 70 ns, and then many dihedral transitions occur in the remaining time. The 70 ns time is correlated with the dihedral and kink dynamics of the helices as mentioned above. Ser 186 is on the E 2 loop which bumps into Helix 7, which is one of the helices with the 70 ns time scale dynamics.

Glu 113 is an important residue that has salt bridge with the N in Lys 296 which is bonded to the retinal. Figure 6 shows that Glu 113 also undergoes a set of dihedral transitions during the 150 ns trajectory for the CB-CD-CG-OE1 dihedral. One of the transition occurs at $t = 70$ ns and is correlated with the Ser 186 dihedral dynamics. Examination of the positions of Ser 186 and Glu 113 during the time period about $t = 70$ ns shows that the dihedral transitions involve the breaking of the salt bridge between Glu 113 and Lys 296 and the formation of hydrogen bonds between Glu 113 and Ser 186. As will be discussed below, these transition involve the presence of water molecules and there hydrogen bond pairing as well.

Figure 7 shows a comparison of the rhodopsin structure at $t = 0$ and 150 ns. Each helix and loop is colored differently to distinguish them. The two states are overlapped and the image is shown in successive 30° rotations. The helices appear to have rotated, but the simulation does not control the rotational diffusion of the protein. The figure gives a visual sense of the degree of tilt and kink angle variation, although one must remember that this is for two instantaneous states, not average states.

Interaction energies

The interaction of retinal with its environment is given in Figure 8. In the calculations of the interaction energies, we take 'retinal' to include Lys 296. It does not make sense to separate the protonated Schiff base, in particular. After isomerization the energy remains at the same average value as before isomerization until just before $t = 70$ ns, where a large rise of about 35 kcal/mol occurs. That the interaction energy does not immediately change upon isomerization is not surprising, given that the isomerization moves the end of the retinal (including the ring) which is not strongly interacting with residues of rhodopsin. The strong interactions occur near the linkage with Lys 296, where salt bridges and strong ionic interactions are present.

A breakdown of retinal's interaction energies with the environment is given in Fig. 9. The breakdown is done both in terms of the interaction type and the molecule type of

the environment. The transition near 70 ns is visible in more than one part of Fig. 9. The protein electrostatic interactions exhibit at large energy rise near $t = 70$ ns. The solvent electrostatic interactions exhibit a similarly size *drop* in energy at the same time. Thus, the net energy change at this transition time is zero. Examination of the retinal interaction with Glu 113, which forms a salt bridge with retinal (the N in Lys 296), shows a sharp transition near $t = 70$ ns. The energy increases by about 40 kcal/mol, which is close to the total energy change of retinal with its environment. Thus, the main source of the transition in Fig. 8 is due to the Glu 113 interaction.

The configurations near $t = 70$ ns were examined for the positions of Glu 113 and Lys 296/retinal along with any nearby water molecules. Figure 10 shows images of 5 different times. At $t = 65$ ns the Glu 113 salt bridge with N of Lys 296 is intact. At $t = 67$ ns, a water molecule is moving in between the residues. By $t = 70$ ns, a group of 3 to 4 water molecules has come into the region. The water molecules diffuse away and by $t = 78$ ns, there is a noticeable gap between the O atoms of Glu 113 and the N atom of Lys 296. By this time the Glu 113 has undergone dihedral transitions which no longer allow short range (salt bridge) interactions to Lys 296.

Conclusions

The preliminary analysis of the long simulation of rhodopsin after isomerization shows that significant structural changes occur in the 150 ns period. The isomerization results in some of the 7 transmembrane helices undergoing tilt and kink angle changes that are well beyond their fluctuation range in the equilibrium dark state. One of the key structural changes is the motion of the ionone ring of retinal. The ring progressively gets closer to Ala 169. This is consistent with crosslink experiments (Borhan 2001) which form a crosslink between the ring and Ala 169.

A strong energetic transition is observed to occur at 70 ns after isomerization. The majority of the energy of this transition involved breaking of the salt bridge between Glu 113 and the protonated Schiff base. Raman spectroscopy (Pan 2001) has shown that the protonated Schiff base stretching modes are indicative of very different Schiff base environments. This implies that the transition from bathorhodopsin to Lumi involves chromophore relaxation and dramatic changes in the Schiff base region. Our results are in agreement with this experimental and data. Furthermore, besides the structural dynamics, we show the connection to the energetics that drives the changes.

References

Sakmar, T., Menon, S., Marin, E. and Awad, E. (2002). Rhodopsin: insights from recent structural studies. Ann. Rev. Biophys. Biomol. Str. 31, 443-484.

L.Shi and Javitch, J. (2002). The binding site of aminergic G protein-coupled receptors: the transmembrane segments and second extracellular loop. Ann. Rev. Pharmacol.42, 437-467.

Filipek, S., Stenkamp, R., Teller, D. and Palczewski, K. (2003). G protein-coupled receptor rhodopsin: a prospectus. Ann. Rev. Physiol. 65, 851-879.

Burns, M. & Baylor, D. (2001). Activation, deactivation, and adaptation in vertebrate, photoreceptor   cells. Ann. Rev. Neurosci. 24, 779-805.

Hubbell, W., Altenbach, C., Hubbell, C. and Khorana, H. (2003).   Rhodopsin structure, dynamics, and activation: a perspective from   crystallography, site-directed spin labeling, sulfhydryl reactivity, and   disulfide cross-linking. Adv. Protein Chem. 63, 243-290.

Ferretti, L., Karnik, S., Khorana, H., Nassal, M. & Oprian, D. (1986). Total synthesis of a gene for bovine rhodopsin. Proc. Nat. Acad. Sci. 83, 599-603.

Fung, B. and Stryer, L. (1980). Photolyzed rhodopsin catalyzes the exchange of GTP for bound GDP in retinal rod outer segments. Proc. Nat. Acad. Sci. 77, 2500-2504.

Sakmar, T., Franke, R. and Khorana, H. (1989). Glutamic acid-113 serves as the retinylidene schiff-base counterion in bovine rhodopsin. Proc. Nat. Acad. Sci. 86, 8309-8313.

Franke, R., Konig, B., Sakmar, T., Khorana, H. and Hofmann, K. (1990). Rhodopsin mutants that bind but fail to activate transducin. Science, 250, 123-125.

Zhukovsky, E. and Oprian, D. (1989). Effect of carboxylic-acid side-chains on the absorption maximum of visual pigments. Science, 246, 928-930.

Yokoyama, S. (2002). Molecular evolution of color vision in vertebrates. Gene, 300, 69-78.

Kuwayama, S., Imai, H., Hirano, T., Terakita, A. and Shichida, Y. (2002).Conserved proline residue at position 189 in cone visual pigments as a determinant of molecular properties different from rhodopsins. Biochemistry, 41, 15245-15252.

Noel, J., Hamm, H. and Sigler, P. (1993). The 2.2-angstrom crystal-structure of transducin-alpha complexed with GTP-gamma-s. Nature, 366, 654-663.

Lambright, D., Noel, J., Hamm, H. and Sigler, P. (1994). Structural determinants for activation of the alpha-subunit of a heterotrimeric G-protein. Nature, 369, 621-628.

Borhan, B., Souto, M., Imai, H., Shichida, Y. and Nakanishi, K. (2000). Movement of retinal along the visual transduction path. Science, 288, 2209-2212.

Pan, D., and R.A. Mathies. (2001) Chromophore structure in lumirhodopsin and metarhodopsinI by time-resolved resonance Raman microchip spectroscopy. Biochemistry 40, 7929-7936.

Crozier, P.S., Stevens, M.J., Forrest, L.R., and Woolf, T.B. (2003). Molecular Dynamics Simulation of Dark-Adapted Rhodopsin in an Explicit Membrane Bilayer: Coupling between Local Retinal and Larger Scale Conformational Change, J. Mol. Bio. 333, 493.

Schlenkrich, M., Brickmann, J., MacKerell, A. D. Jr. and Karplus, M. (1996). An empirical potential energy function for phospholipids: criteria for parameter optimization and applications. In *Biological membranes: A molecular perspective from computation and experiment.*, (Merz, K.M. Jr., and Roux, B., eds), pp. 31-81. Birkhauser Press.

MacKerell, A., Bashford, D., Bellott, M., Dunbrack, R., Evanseck, J., Field, M., Fischer, S., J, J.G., Guo, H., Ha, S., Joseph-McCarthy, D., Kuchnir, L.,

Kuczera, K., Lau, F., Mattos, C., Michnick, S., Ngo, T., Nguyen, D., Prodhom, B., Reiher, W., Roux, B., Schlenkrich, M., Smith, J., Stote, R., J.Straub, M, M.W., Wiorkiewicz-Kuczera, J., Yin, D. & Karplus, M. (1998). All-atom empirical potential for molecular modeling and dynamics studies of proteins. J Phys. Chem. B, 102, 3586-3616.

Nina, M., Smith, J. & Roux, B. (1993). Ab-initio quantum-chemical analysis of schiff-base water interactions in bacteriorhodopsin. Theochem-journal of molecular structure, 105, 231-245.

Palczewski, K., Kumasaka, T., Hori, T., Behnke, C.A., Motoshima, H., Fox, Trong, I.L., Teller, D.C., Okada, T., Stenkamp, R.E., Yamamoto, M., and Miyano, M. (2000) Crystal structure of rhodopsin: a G protein-coupled receptor, Science, 289 739-745.

Plimpton, S.J., (1995) Fast parallel algorithms for short-range molecular dynamics. J. Comp. Phys., 117, 1-19.

Figure 1 Retinal dihedral angles as a function of time. The blue line represent the dynamics for the 40 ns run of the dark adapted rhodopsin, *i.e.* retinal in the *cis* state and the C11-C12 dihedral has angle 0. The red line represent the dynamics after the *cis-trans* isomerization, *i.e.* retinal is in the *trans* state with the angle at 180 (=-180).
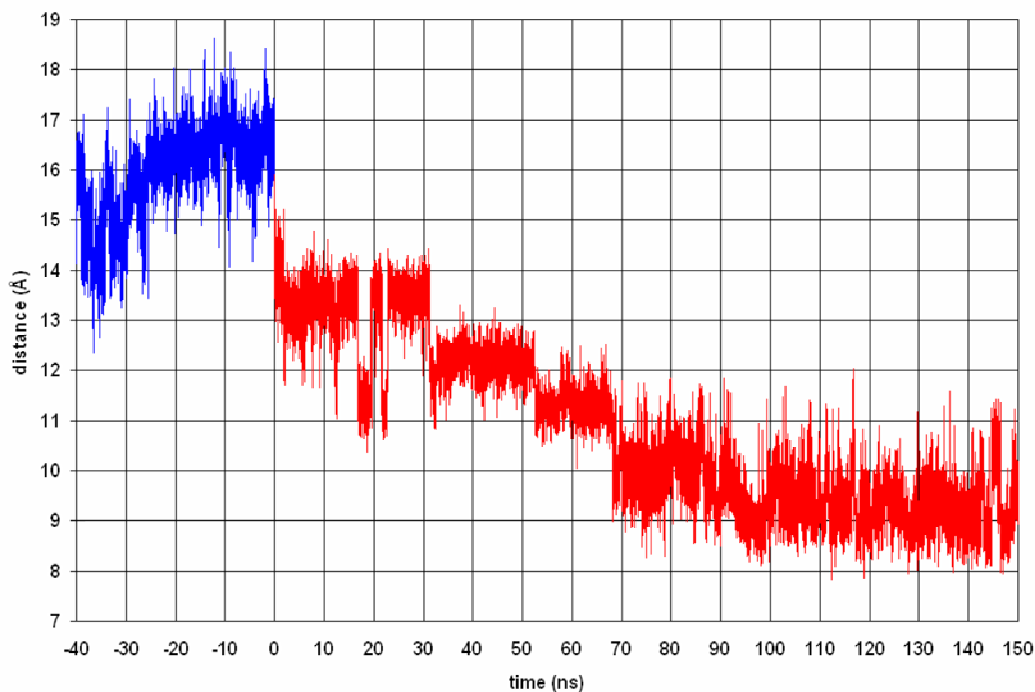
Figure 2 The distance between retinal's ionone ring and Ala 169. The blue line represent the dynamics for the 40 ns run of the dark adapted rhodopsin, *i.e.* retinal in the *cis* state. The red line represent the dynamics after the *cis-trans* isomerization, *i.e.* retinal is in the *trans* state.

16

Figure 3 Tilt angles as a function of time for Helices 5b, 5c, 6b and 7a. The blue lines represent the tilt angle dynamics for the 40 ns run of the dark adapted rhodopsin, *i.e.* retinal in the *cis* state. The red lines represent the dynamics after the *cis-trans* isomerization, *i.e.* retinal is in the *trans* state.
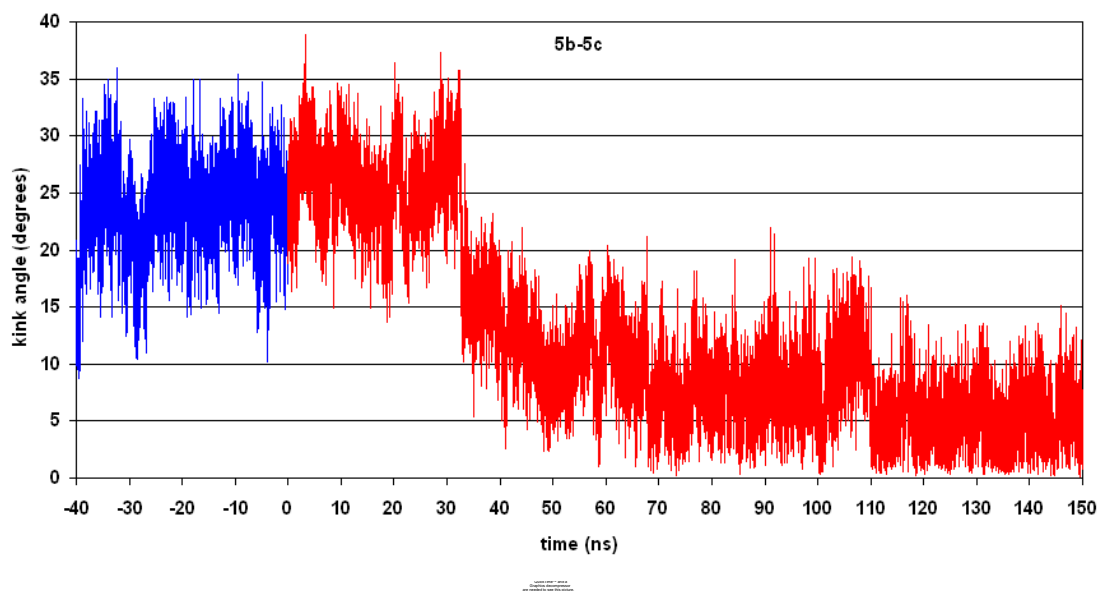
Figure 4 Kink angles as a function of time for Helices 5b-5c and 6a-6b. The blue lines represent the dynamics for the 40 ns run of the dark adapted rhodopsin, *i.e.* retinal in the *cis* state. The red lines represent the dynamics after the *cis-trans* isomerization, *i.e.* retinal is in the *trans* state.
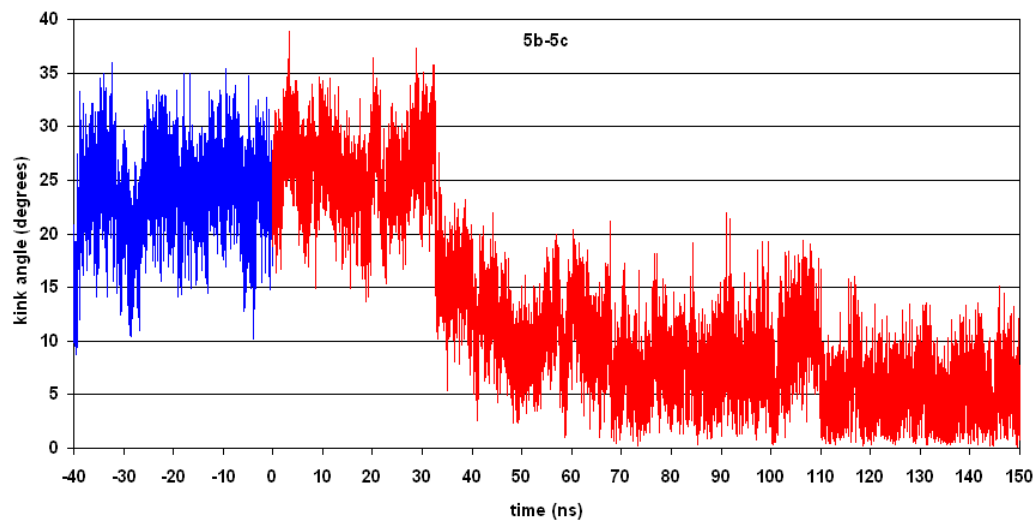
Figure 5 Kink angles as a function of time for helices 5b-5c and 6a-6b. The blue lines represent the dynamics for the 40 ns run of the dark adapted rhodopsin, *i.e.* retinal in the *cis* state. The red lines represent the dynamics after the *cis-trans* isomerization, *i.e.* retinal is in the *trans* state.

19
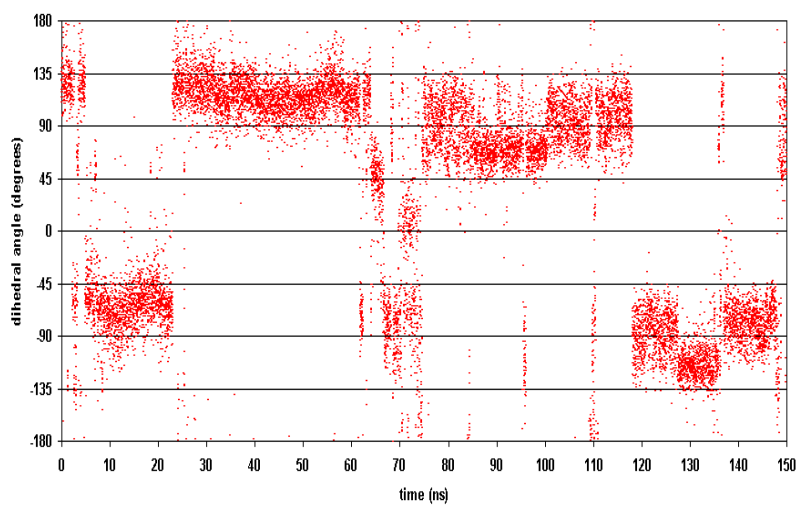
Figure 6 Dihedral angles as a function of time for side chains of Ser 186 and Glu 113. The blue line represent the dynamics for the 40 ns run of the dark adapted rhodopsin, *i.e.* retinal in the *cis* state. The red line represent the dynamics after the *cis-trans* isomerization, *i.e.* retinal is in the *trans* state.

Rhodospin postisomerization: t = 0 & 150ns states

helix	color	helix	color
1	blue	5	tan
2	red	6	green
3	orange	7	cyan
4	yellow	8	purple
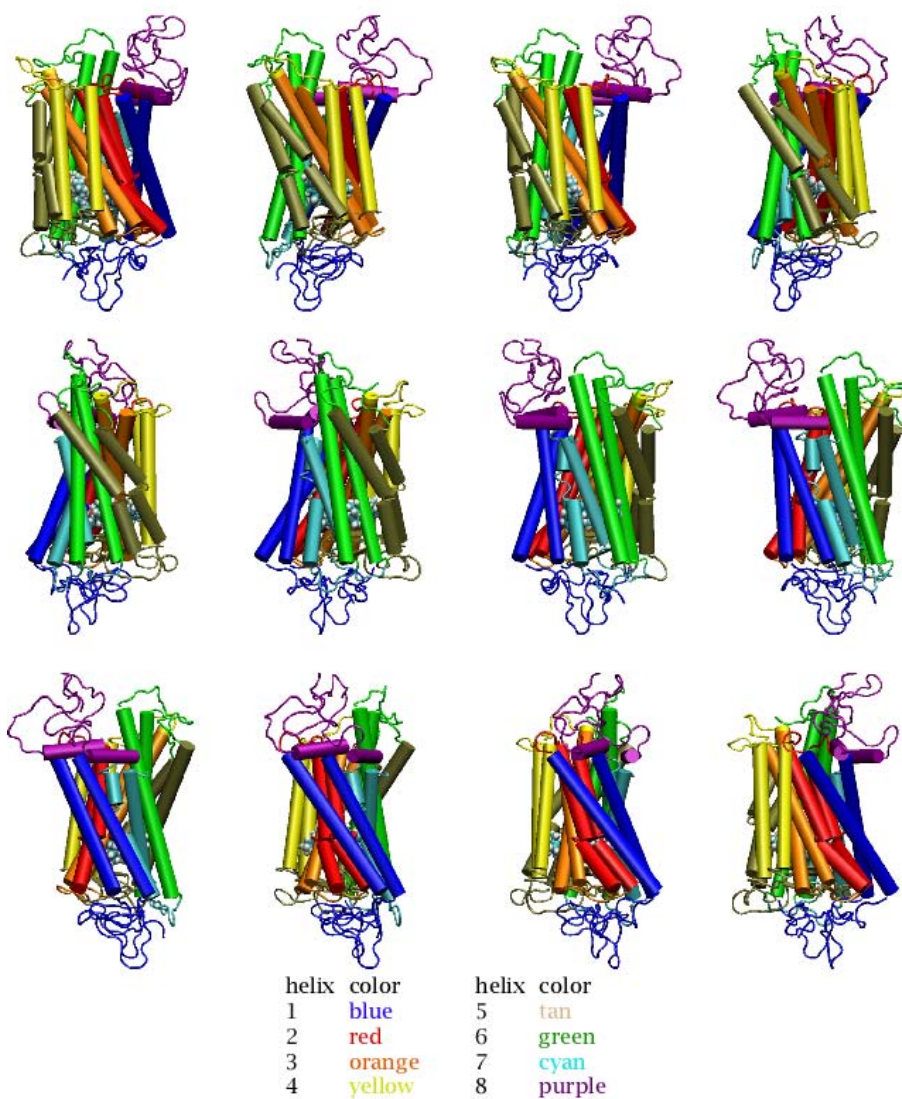
Figure 7 Overlap of images of rhodopsin protein at $t = 0$ and 150 ns. The sequence of images is the set of 30° rotations about the z-axis.

QuickTime™ and a
Graphics decompressor
are needed to see this picture.

Figure 8 Interaction energy between retinal and its environment.

QuickTime™ and a
Graphics decompressor
are needed to see this picture.

Figure 9 Interaction energy between retinal and its environment split into different interaction types and different environment molecules.

t = 65 ns

t = 67 ns

t = 70 ns

t = 72 ns

t = 78 ns
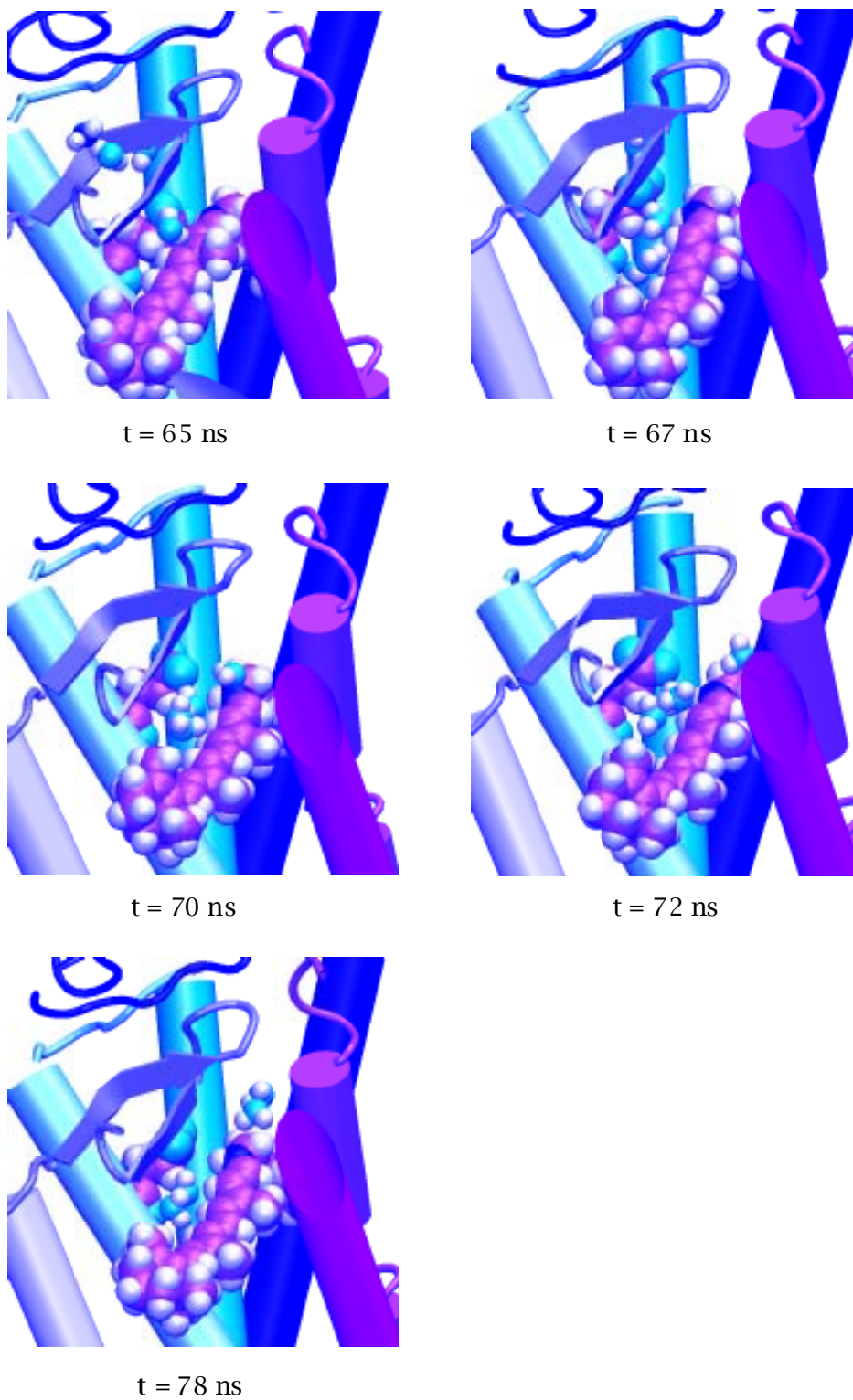
Figure 10 Images of the rhodopsin protein, Glu 113, retinal, Lys 296 and selected waters. Glu 113, Lys 296 and retinal are shown in vdW mode. Four water molecules are shown in a shrunken vdW representation. The labels give the time of the snapshot images.

Chapter 3 Comparison between isolated rhodopsin helices simulations and intact rhodopsin simulation

Paul S. Crozier[1], Mark J. Stevens[2], Joseph S. Schoeniger[3], and Thomas B. Woolf[4]

Affiliations:
1) Sandia National Laboratories, P.O. Box 5800, MS 0310, Albuquerque, NM 87185-0310, USA
2) Sandia National Laboratories, P.O. Box 5800, MS 1411, Albuquerque, NM 87185-1411, USA
3) Sandia National Laboratories, MS 9951, Livermore, CA 94550-9951, USA
4) Department of Physiology, Johns Hopkins University, School of Medicine, Baltimore, MD 21205, USA

Abstract: The seven transmembrane helices of bovine rhodopsin are examined via molecular dynamics simulation, with comparison of helix characteristics as simulated in intact rhodopsin verses simulation of the isolated helices. The all-atom molecular dynamics simulations included explicit lipid bilayers and explicit solvent molecules in all cases, and were 20 nanoseconds each for the isolated helix simulations and 40 nanoseconds for the intact rhodopsin simulation. The simulations show that helix behavior is strongly dependent on the rest of the protein to determine the helix tilt, kink, and secondary structure characteristics. Key elements of secondary structure that are present in native rhodopsin were maintained in the intact rhodopsin simulation, but were absent in the isolated helix simulations due to the lack of the inter-helical interactions and the loop:helix interactions that are needed in order to form and maintain the native secondary structure.

Introduction

Even though membrane proteins are extremely important to cell function and make up 20-30% of the genome,[1] few well-defined structures of membrane proteins have been published owing partly to the difficulty of membrane protein crystallization. The dark-adapted form of bovine rhodopsin is a notable exception[2-3] and provides considerable insight into the structure and function of a large class of membrane proteins. The protein folding problem is especially difficult in the case of membrane proteins since the mechanism of assembly is not entirely clear and involves the membrane. It has been postulated that individual transmembrane helices form first, followed by formation of the native transmembrane helix bundle conformation.[4] This presupposes that transmembrane helices are independently stable units of secondary structure, and raises the question: if isolated, do individual transmembrane helices maintain native conformation, or are their structures highly dependent on the remainder of the protein? This article addresses this and other relevant questions via molecular dynamics (MD) simulation of isolated transmembrane helices from rhodopsin as well as MD simulation of the known structure of intact dark-adapted rhodopsin.

Goddard's group built models of membrane proteins using a computational approach, where transmembrane regions were predicted, and idealized α–helices built and optimized using torsional MD.[5] Further refinement of their model included all-atom MD simulation in an explicit lipid bilayer using the MPSim software.[6] Their successes have provided motivation for our exploration of the hypothesis that simulation of isolated alpha helices can be used to predict helix irregularities. However, we show that isolated helix simulation cannot be used for accurate prediction of helix tilts, kinks, and secondary structure characteristics. Since the other helices and loops of the given transmembrane protein strongly affect helix structure, they must be included in simulations used to predict helix structural characteristics.

Biggin and Sansom give an excellent summary of α–helix simulation studies in their 1999 review article.[7] Here, we give a brief overview of recent work specific to all-atom simulation. Previous MD studies of isolated helices have, to a limited degree, demonstrated the ability to predict membrane protein secondary structure, including kinks, bends, and tilts. Bright *et al.*,[8] Cordes *et al.*,[9] and Bright *et al.*[10] have shown that helix distortions induced by proline and glycine motifs can be studied by MD simulation of isolated helices in a membrane-mimetic biphasic octane/water system. Woolf[11-13] performed all-atom MD simulation of isolated bacteriorhodopsin helices in an explicit dimyristoyl phosphatidylcholine (DMPC) lipid environment. Due to the CPU-intensive nature of all of the calculations mentioned above, each was limited in terms of simulation time (up to a 1.0 ns each), lipid to helix ratio (12:1), and long-range electrostatics (12 Å cutoff). In contrast, the isolated helix simulations of the present study are 20 ns in duration, had a lipid-to-helix ratio of 30:1, and use the particle-particle/particle-mesh (P^3M) Ewald long-range electrostatics method.

Methods

Rather than perform simulations of isolated helices in a vacuum, a mean field environment, or a membrane-mimetic environment,[8] we have performed these simulations in an explicit dioleoyl phosphatidylcholine (DOPC) lipid environment immersed in an aqueous (TIP3P) ionic (NaCl) environment. This has the advantage of a much more accurate description of the interfacial region between the aqueous phase and the hydrophobic core of the lipid bilayer. No approximation to hydrophobic matching is needed and fluctuations of the hydrophobic region are allowed. Also avoided are problems associated with inadequate modeling of the environmental viscosity that likely influences the bending dynamics of the transmembrane helices. The disadvantage of including the lipid and solvent environments in atomistic detail is that these simulations are very computationally demanding.

Long-range electrostatics calculations can also be computationally demanding. But inadequate representation of the long-range electrostatics can introduce unwanted artifacts, so we have used full P^3M Ewald electrostatics to avoid errors associated with cutoff electrostatics.[14-15]

Good lipid mixing and system equilibration are difficult to achieve on the currently feasible nanoseconds time scale of all-atom molecular simulation. In an effort to reduce time scale concerns, we have built ensembles from pre-equilibrated lipids according to the protocol established by Woolf and Roux[16] to minimize the needed equilibration time, and performed relatively long time scale simulations of 20 nanoseconds for each isolated transmembrane helix. Initialization and equilibration was done using the CHARMM molecular modeling package, and subsequently, each simulation required approximately 20 CPU days on 12 processors of CPlant[17] using the LAMMPS[18] parallel MD software package.

The seven transmembrane helices of rhodopsin were defined as the residues given in Table 1. We followed the procedure of Woolf and Roux[16] to set up the membrane protein ensembles in an explicit lipid bilayer. A brief description of the procedure follows. Each isolated helix simulation was initialized by placement of the idealized helix perpendicular to the membrane surface and centered in the membrane. DOPC lipid molecules were then chosen at random from a pre-equilibrated library of lipids created from a pure lipid bilayer simulation. Lipids were fitted around the protein and rotation and translation moves were performed to minimize atom overlaps, which were then followed by energy minimization. Following construction of the lipid bilayer around the isolated helix, each system was immersed in TIP3P water and NaCl ions were added to neutralize the net system charge and achieve ~0.1 M salt bath solution. After relaxation by further energy minimization, equilibration dynamics were performed for 25 ps.

All simulations were performed at a constant temperature of 307 K and at a constant pressure of 1 atm using a Nosé-Hoover thermostat/barostat. In order to maintain a constant membrane surface area, the simulation box was allowed to fluctuate only in the direction perpendicular to the membrane, with the box dimensions in the other two directions held constant. After initial equilibration, production runs of 20 ns for each of the seven isolated transmembrane helices were performed for comparison with a 40 ns intact rhodopsin simulation performed under similar conditions and reported elsewhere.[19]

In order to allow motion free of artificially imposed restraints, none of the isolated helix ends were tethered, nor were the backbone atoms fixed in place after the initial equilibration. With no restraints imposed, it will be shown that the isolated helices have a tendency to unravel near the ends and to degenerate away from the initial α-helix conformation.

Results

The simulation time frame of 20-40 ns is adequate to observe a great deal of helix motion, especially in the case of the isolated helix simulations. Substantial changes in helix tilt, kink, conformation, and energetics were observed, with much larger changes seen in the isolated helices than in the intact rhodopsin helices. Although the isolated helix simulations were initialized with each helix placed perpendicular to the membrane in the idealized α−helix conformation, the helices quickly devolved into less ordered structures with large tilt and kink angles. Large changes in helix conformation continued to occur throughout the entire 20 ns of each isolated helix simulation, signaling that the equilibrium ensemble has not necessarily been reached, since the simulation moves far from the starting structure. This behavior is not unlike that observed in other isolated helix simulations,[7-13,16,20] although the present simulations give a longer and more complete picture.

Helix Tilt and Kink Angles

Figures 1 and 2 display tilt and kink angles of the transmembrane helices from the intact rhodopsin simulation on the left and the isolated helix simulations on the right. The tilt angle, defined as the angle between the *z*-axis, perpendicular to the membrane surface, and the major axis for the cylinder that best fits the helix, were computed for each snapshot and plotted as a function of time in Figure 1. For the kink angles, sections of each helix above and below each kink point were fit to cylinders and the kink angle was defined as the angle between the axes of the contiguous cylinders on the same α−helix. Kink angles are plotted as a function of time in Figure 2, with the hinge point residue for each kink listed in the caption. Experimentally measured tilt and kink angles are marked with an arrow and a straight line, representative of the angles computed from the static x-ray structure of rhodopsin.

Tilt angle fluctuations on the picosecond time scale are on the order of a few degrees in both the intact rhodopsin simulation and in the isolated helix simulations. However, over the course of the simulation, the range between the minimum and maximum tilt angle in the intact rhodopsin simulation is approximately 15° for each helix, while the range between the minimum and maximum tilt angle in the corresponding isolated helix simulations is 45°±5° and would likely be larger if the simulations were continued. The large range for the isolated helix simulations can partly be attributed to the fact that the isolated helix simulations were started with the helices perpendicular to the membrane, whereas in the case of the intact rhodopsin simulation, the helices were initialized in their known x-ray structure positions. In particular, isolated helices 3 and 5 achieve tilt angles close to the crystal values (Figure 1).

However, for helices 4 and 7, the trend was almost entirely away from the experimentally measured tilt angle. The tilt angle of isolated helix 1 is steadily increasing and deviates from the crystal value by 7° at the end of the run.

Correspondingly, the deviations from the experimentally measured tilt angles were much larger for the isolated helices than for the helices in the intact rhodopsin. The absolute value of the difference between the simulated tilt angle and the experimentally measured tilt angle, as averaged over all 7 transmembrane helices for each snapshot, was 5° for the intact rhodopsin simulation, while it was 17° for the isolated helix simulations. Likewise, examining just the endpoint snapshot reveals that the intact rhodopsin simulation helix tilt angles varied from the experimentally measured tilt angles by an average of only 5°, whereas they varied by an average of 19° in the isolated helix simulations.

Similar to the tilt angles, fast fluctuations in kink angles are on the order of a few degrees in both the intact rhodopsin simulation and in the isolated helix simulations (Figure 2). However, again, the ranges between the minimum and maximum kink angles in the isolated helix simulations are much larger than in the intact rhodopsin simulation, indicating much more freedom of motion around kinking residues in the case of the isolated helix simulations. Isolated helices 1 and 3(b) have kink angles similar to the corresponding intact rhodopsin helices, albeit with larger fluctuations. By the end of the simulation, isolated helix 3(a) has relaxed to the same value as the intact rhodopsin helix 3(a), although it is not clear that it would have remained at that value if the run had been continued even longer. Isolated helices 2, 6, and 7 differ significantly from the corresponding intact rhodopsin helices.

Very large kink angles occurred in some of the isolated helices, but almost never exceeded 45° in the intact rhodopsin. We show an example of a very large kink angle in Figure 3, where the simulation of isolated helix 2 produced a kink centered on Ala 80. Interestingly, no kink formed around Gly 89 and Gly 90 as in the native rhodopsin structure. Without the constraints at either end of the helix and without the hydrogen bonding networks of the neighboring helices that are present in native rhodopsin, the isolated helix is free to kink in a different location and to solvent match. The helix exhibits exaggerated kinking in a non-native location in order to minimize contact of hydrophobic residues with water and hydrophilic residues with the lipid tails.

HELANAL Classifications

Kumar and Bansal[21-22] have devised a system for dividing α–helices into kinked, curved, or linear classifications, and have shown that almost all α–helices fall into these categories. We have used HELANAL, their analysis program, to classify each helix snapshot from the simulations as kinked, curved, linear, or ambiguous. The present simulations show that the individual helices of rhodopsin are primarily classified as kinked, but for a small fraction of snapshots during the course of the simulations are better classified as curved or linear.

According to the HELANAL classification system, kinked helices are characterized by local bending angles greater than 20°. Linear and curved helices have no local bending angles greater than 20°, and the average of their local bending angles is less than

10º. A helix is considered linear rather than curved if a fit to a straight line is better than a similar root-mean-squared deviation (RMSD) fit to an arc. If the fit to an arc is better, the helix is considered curved rather than linear.

Due to the fact that each of the transmembrane helices in rhodopsin has at least one kink-inducing residue, rhodopsin's helices predominately exist in a kinked state. It has been speculated that kinks act as molecular hinges that allow membrane proteins to undergo conformational changes necessary for signaling.[8-9] Kinks in rhodopsin's helices are likely important for conformational changes during photoisomerization.[19] HELANAL classifies all of the transmembrane helices in both the intact rhodopsin and the isolated helices simulations as kinked during the vast majority of the simulated time. Non-kinked behavior was distributed fairly evenly across the time frame of each of the simulations rather than distributed as blocks of non-kinked time. In the intact rhodopsin simulation, only Helices 1, 3, and 5 exhibited substantial curved helix behavior (0.15, 0.18, and 0.01 probability, respectively), with Helix 3 being the only helix to exhibit some linear behavior (0.07 probability). In contrast, the isolated helix simulations showed an even greater majority of kinked helix behavior, with only Helices 1 and 4 showing some curved helix behavior (0.02 and 0.09 probability, respectively), and only Helix 4 showing a small fraction of linear helix behavior (0.01 probability).

Overall, the HELANAL analysis points to the fact that the presence of the entire intact membrane protein is needed in order to maintain the native helix geometric configurations. This conclusion is further reinforced and by the analysis at the residue level that follows.

DSSP Comparisons

In addition to examining each of the helices in its entirety in terms of its overall shape, we have examined the individual residues of each helix in terms of its predominate secondary structure characteristics using the Define Secondary Structure of Proteins (DSSP) program of Kabsh and Sander.[23] Secondary structure for each of the simulated helices was computed as a function of time, giving a dynamic picture of the secondary structure of each residue of each helix, as shown in Figure 4. Overall, the isolated helices exhibited much less order in their structure than did the helices in intact rhodopsin (especially helices 3 and 6). Helix 7 is the notable exception.

The isolated helices were initiated as completely idealized α–helices, but they quickly departed from that state, showing kinking, turns, and unraveling, particularly at the ends. Even though unraveling progressed somewhat over the course of the simulations, in general, it appears that a reasonably stable steady state has been achieved. Irregular helix formation, involving 3_{10} helices and π-helices, occurs much more frequently in the isolated helix simulations than in the intact rhodopsin simulations. While some of this behavior can be attributed to force field inadequacies, it is not uncommon to observe overcoiling or undercoiling near the ends of α–helices in their native structures.[24]

As noted previously, a simulated isolated rhodopsin helix can have kinks present that are not observed in the corresponding intact rhodopsin helix. Likewise, a kink present in the intact rhodopsin will not necessarily be present in the corresponding

isolated helix simulation. A great deal of helix distortion and unraveling near the ends was observed in the isolated helix simulations and not in the intact rhodopsin helices. The following paragraphs discuss in more detail specific differences observed between each helix in the isolated and intact simulations.

Helix 1 is nearly ideal and has very little kinking near Pro 53 both in the intact rhodopsin simulation and in the isolated helix simulation. In general, the presence of proline correlates with α-helix distortion, but very little distortion occurs in this case. Even less distortion occurred around Pro 53 in the isolated helix simulation than in the intact rhodopsin simulation. This is in contrast to the large and growing α-helix distortion at either end of the α-helix in the isolated helix simulation, where it tends to degenerate into π-helix and hydrogen bonded turn regions. The isolated Helix 1 is very different from the intact rhodopsin Helix 1, primarily at the ends. The intact rhodopsin helix does not become non-helix until Glu 33 on the extracellular side and His 65 on the cytoplasmic side. In contrast, the isolated helix becomes non-helical from Phe 37 to the extracellular compartment and from Leu 59 to the cytoplasmic compartment, even unraveling down to Pro 53 at some times. The intact rhodopsin helix exhibits a kink at Pro 53, which shows up as "H-bonded turn" at Phe 52 in Figure 4a. This kink is also hinted at in the isolated Helix 1 simulation, but is less distinct and shifted slightly, as seen by the faint "H-bonded turn" between residues 50 and 52 in Figure 4b.

The only proline residue in Helix 2 is Pro 71, found near the cytoplasmic end of the helix. Pro 71 causes similar kinking distortion in the intact rhodopsin simulation and in the isolated helix simulation. But kinking near Pro 71 is mild compared to the major kinking center found in native rhodopsin Helix 2 centered on Gly 89 and Gly 90. Kinking around these two glycines is noticeably absent in the isolated helix simulation. The major kink found in the intact rhodopsin simulation centered on Gly 89 and Gly 90 places Gly 90 close to the Schiff base, Glu 113 of Helix 3. In the absence of Helix 3 and the rest of rhodopsin, no kink forms around Gly 89 and Gly 90, indicating that the tertiary structure holds the secondary structure in place. In native rhodopsin, the structure of Helix 2 is influenced by inter-helical H-bonding networks involving Asp 83 and Asn 78.[2] In contrast to the intact rhodopsin simulation of Helix 2, the isolated Helix 2 simulation exhibits kinking in the region near Ala 80 rather than in the region near Gly 90. The DSSP analysis of intact rhodopsin Helix 2 implies that it consists of residues 73 to 100 with 88-91 being non-helical, but maintaining the H-bonded turn structure, which is fairly constant throughout the simulation (Figure 4c). The isolated helix is different on the extracellular end, where for t > 8 ns, residues 96-99 tend to be either an H-bonded turn or a π-helix (Figure 4d). The cytoplasmic end of the isolated helix is only slightly different from the intact helix of the same residue range. The kink that is evidenced by a few residues of non-helical H-bonded turn moves to residues 77-81 in the isolated helix.

Helix 3 in intact rhodopsin is almost entirely α−helical, while the simulation of isolated Helix 3 shows a great deal of kinking and non-ideality according to the DSSP analysis (Figure 4f). Gly 120 and Gly 121 do not distort Helix 3 in the intact rhodopsin simulation, but cause a distinct kink in the simulation of isolated Helix 3. Likewise, a turn occurs near Glu 113 and Gly 114 in the isolated helix but is entirely absent in the intact rhodopsin simulation. Helix 3 exhibits the opposite behavior of Helix 2, in that it has no kinking around glycines in the intact rhodopsin simulations but does kink around glycines in the isolated helix simulations.

The simulations of intact and isolated Helix 4 are much more similar to each other (Figures 4g and 4h). The two adjacent proline residues, Pro 170 and Pro 171 induce a non-helical region with no inter-residue hydrogen bonds (labeled "bend" by DSSP) in Helix 4, which appears in the DSSP analyses as a bend at Ala 169. The bend is more pronounced and focused on Ala 169 in the intact rhodopsin simulation, and residues 169-173 are more floppy in the isolated helix simulation. The cytoplasmic side of isolated Helix 4 shows H-bonded turns from residue 150 to 152 at early times and H-bonded turns or π−helix from residues 150 to 157 at late times. This behavior is not seen at all in the intact rhodopsin simulation of Helix 4.

Kinking in Helix 5, induced in part by Pro 215, is evidenced by a H-bonded turn region seen near Phe 212 in both the isolated helix simulation and in the intact rhodopsin simulation, but is more pronounced in the intact rhodopsin simulation (Figures 4i and 4j). In the isolated helix simulation, the extracellular end of Helix 5 near Glu 201 and Ser 202 begins as part of the α−helix, but devolves into a H-bonded turn region after about 6.5 ns. Similar behavior occurs on the cytoplasmic end of Helix 5. After 15 ns, undercoiling of Helix 5 transforms the region from residues 221 to 225 into a π−helix. This may be at least partially due to inadequacies in the CHARMM 22 force field, which has a tendency to favor π−helices in structures that should be α−helices.[24]

From the rhodopsin x-ray structure (Ref. 2, p. 741), it can be observed that Phe 293 and Phe 294 of Helix 7 interact with Leu 40 of Helix 1 and Cys 264 of Helix 6, and that this interaction is likely important to rhodopsin function since it is facilitated by the distortion of Helix 6 in the region around Ile 263. Both the intact rhodopsin simulation and the isolated helix simulation show a large kink with a highly variable kink angle near Ile 263 (Figure 2). Interestingly, the DSSP analysis shows considerable helix distortion around Ile 263 in the isolated helix simulation, but the intact rhodopsin simulation shows only very faint distortion of the α−helical structure of Helix 6, even with the kink present. The DSSP analysis shows that the intact rhodopsin helix is characterized as almost entirely α−helical, while the isolated Helix 6 shows π−helix formation near the cytoplasmic end, as seen in Helix 5. Interestingly, in this case, the π−helix transforms back into an α−helix before the end of the simulation.

Helix 7 of intact rhodopsin has a much richer structure than the other intact rhodopsin helices and contrasts substantially from the isolated helix. The center section of Helix 7 is primarily non-helical, with Thr 297 and Ser 298 in an unstructured region for nearly the entire simulation. Residues 299-301 are classified as a H-bonded turn region. Ala 295 and Lys 296 are primarily designated H-bonded turn residues, except in the period from 11 to 24 ns, when they usually form part of a tightly coiled 3_{10}-helix. None of this middle structure is present in the isolated helix; it is characterized as helical for the entire simulation (Figure 4n). After 12 ns, the α−helical region near the extracellular end actually grows, while the opposite occurs at the cytoplasmic end of the helix. Again, we see frequent π-helix formation in the isolated helix simulation, this time including the region between Asn 302 and Met 308.

Conclusion

Simulations of isolated helices have been compared against the corresponding intact rhodopsin simulation from the level of the entire helix down to the structural details of the individual residues that make up the helices. These relatively long time scale simulations have shown that helix characteristics slowly evolve and require a long time to equilibrate. In all seven rhodopsin transmembrane helices, very substantial structural differences were observed between the isolated helix simulations and the intact rhodopsin simulation. The observed differences are due to the unraveling of the untethered ends in the isolated helix simulations and the effects of the rest of the rhodopsin molecule beyond the helix in question, which plays a key role in maintaining helix secondary structure through disulfide bridges, hydrogen bonding networks, and non-bond inter-atomic interactions.

It does not appear to be possible to use isolated helix simulations to predict membrane protein helix structures, even if simulated in a native-like lipid environment. We have demonstrated that expensive all-atom simulations of idealized individual transmembrane helices give little useful information about native helix conformations. The rest of the protein, with its tertiary structure, is required to enforce the helix secondary structure. Solvent matching alone is a necessary, yet insufficient, condition for tilt and kink angle determination or for proper folding.

Reasonably favorable comparisons between the isolated helix simulations and the intact rhodopsin simulation were shown for the tilt angles of Helices 3 and 5, the kink angles of Helices 1 and 3, the HELANAL comparison of Helices 2, 5, 6, and 7, and the DSSP comparison of Helices 1, 4, and 5. But since it is difficult to anticipate the favorable predictions we must conclude that simulation of isolated helices, even with high fidelity all-atom MD, has poor helix characteristic prediction capability.

We recommend helix bundling and coarse-grained rigid body MD of the helix bundle in the lipid environment prior to all-atom MD relaxation of the helices. Such a procedure provides the correct environment for the individual helices that includes the other helices and the loop regions, which strongly affect the secondary structure of the individual helices.

References

1. Erik Wallin and Gunnar Von-Heijne, *Genome-wide analysis of integral membrane proteins from eubacterial, archaean, and eukaryotic organisms,* Protein Science, 7 (1998) 1029-1038.
2. Krzysztof Palczewski, Takashi Kumasaka, Tetsuya Hori, Craig A. Behnke, Hiroyuki Motoshima, Brian A. Fox, Isolde Le Trong, David C. Teller, Tetsuji Okada, Ronald E. Stenkamp, Masaki Yamamoto, and Masashi Miyano, *Crystal structure of rhodopsin: a G protein-coupled receptor*, Science, 289 (2000) 739-745.
3. David C. Teller, Tetsuji Okada, Craig A. Behnke, Krzysztof Palczewski, and Ronald E. Stenkamp, *Advances in determination of a high-resolution three-dimensional structure of rhodopsin, a model of G-protein-coupled receptors (GPCRs)*, Biochemistry, 40 (2001) 7761-7772**.**
4. Jean-Luc Popot and Donald M. Engelman, *Membrane protein folding and oligomerization: the two-stage model,* Biochemistry, 29 (1990) ₋₋.
5. Nagarajan Vaidehi, Wely B. Floriano, Rene Trabanino, Spencer E. Hall, Peter Freddolino, Eun Jung Choi, Georgios Zamanakos, and William A. Goddard III, *Prediction of structure and function of G protein-coupled receptors*, Proceedings of the National Academy of Sciences of the United States of America, 99 (2002) 12622-12627.
6. Kian-Tat Lim, Sharon Brunett, Mihail Iotov, Richard B. McClurg, Nagarajan Vaidehi, Siddharth Dasgupta, Stephen Taylor, and William A. Goddard III, *Molecular dynamics for very large systems on massively parallel computers: the MPSim program*, Journal of Computational Chemistry, 18 (1997) 501-521.
7. Phil C. Biggin and Mark S. P. Sansom, *Interactions of α−helices with lipid bilayers: a review of simulation studies*, Biophysical Chemistry, 76 (1999) 161-163.
8. Joanne N. Bright, Indira H. Shrivastava, Frank S. Cordes, and Mark S. P. Sansom, *Conformational dynamics of helix S6 from Shaker potassium channel: simulation studies,* Biopolymers, 64 (2002) 303-313.
9. Frank S. Cordes, Joanne N. Bright, and Mark S. P. Sansom, *Proline-induced distortions of transmembrane helices,* Journal of Molecular Biology, 323 (2002) 951-960.
10. Joanne N. Bright and Mark S. P. Sansom, *The flexing/twirling helix: exploring the flexibility about molecular hinges formed by proline and glycine motifs in transmembrane helices,* The Journal of Physical Chemistry B, 107 (2003) 627-636.
11. Thomas B. Woolf, *Molecular dynamics of individual α−helices of bacteriorhodopsin in dimyristoyl phosphatidylcholine. 1. Structure and dynamics,* Biophysical Journal, 73 (1997) 2376-2392.
12. Thomas B. Woolf, *Molecular dynamics simulations of individual α−helices of bacteriorhodopsin in dimyristoylphosphatidylcholine. II. interaction energy analysis,* Biophysical Journal, 74 (1998) 115–131.

13. Thomas B. Woolf, *Bacteriorhodopsin α–helices in lipid settings: insights for structure prediction,* International Journal of Quantum Chemistry, 69 (1998) 105-116.
14. Gabriela S. Del Buono, Terry S. Cohen, and Peter J. Rossky, *Effects of long-range interactions on the dynamics of ions in aqueous solution,* Journal of Molecular Liquids, 60 (1994) 221-236.
15. S. G. Kalko, G. Sese, and J. A. Padro, *On the effects of truncating the electrostatic interactions: Free energies of ion hydration,* Journal of Chemical Physics 104 (1996) 9578-9585.
16. Thomas B. Woolf and Benoit Roux, *Molecular dynamics simulation of the gramicidin channel in a phospholipid bilayer,* Proceedings of the National Academy of Sciences of the United States of America, 91 (1994) 11631-11635.
17. Ron Brightwell, Lee Ann Fisk, David S. Greenberg, Tramm Hudson, Mike Levenhagen, Arthur B. Maccabe, Rolf Riesen, *Massively parallel computing using commodity components,* Parallel Computing, 26 (2000) 243-266.
18. Steven J. Plimpton, *Fast parallel algorithms for short-range molecular dynamics,* Journal of Computational Physics, 117, (1995) 1-19.
19. Paul S. Crozier, Mark J. Stevens, Lucy R. Forrest, and Thomas B. Woolf, *Molecular dynamics simulation of dark-adapted rhodopsin in an explicit membrane bilayer: coupling between local retinal and larger scale conformational change,* Journal of Molecular Biology, 333 (2003) 493-514.
20. Lucy R. Forrest, D. Peter Tieleman, and Mark S. P. Sansom, *Defining the transmembrane helix of M2 protein for influenza A by molecular dynamics simulations in a lipid bilayer,* Biophysical Journal, 76 (1999) 1886-1896.
21. Sandeep Kumar and Manju Bansal, *Structural and sequence characteristics of long α–helices in globular proteins,* Biophysical Journal, 71 (1996) 1574-1586.
22. Sandeep Kumar and Manju Bansal, *Geometrical and sequence characteristics of α–helices in globular proteins,* Biophysical Journal, 75 (1998) 1935-1944.
23. Wolfgang Kabsh and Christian Sander, *Dictionary of protein secondary structure: pattern recognition of hydrogen-bonded and geometrical features*, Biopolymers, 22 (1983) 2577-2637.
24. Michael Feig, Alexander D. MacKerell, Jr., and Charles L. Brooks, III, *Force field influence on the observation of π-helical protein structures in molecular dynamics simulations*, The Journal of Physical Chemistry B, 107 (2003) 2831-2836.

Helix	First residue	Last residue
1	33	65
2	70	101
3	105	140
4	149	173
5	199	226
6	245	278
7	284	309

Table 1. Rhodopsin residues included in each of the seven transmembrane isolated helix simulations.

Figure 1. Helix tilt angles as a function of time are shown with the intact rhodopsin helices on the left and the isolated helices on the right. Static experimentally-measured tilt angles are marked by the flat lines and by the arrows on the right.
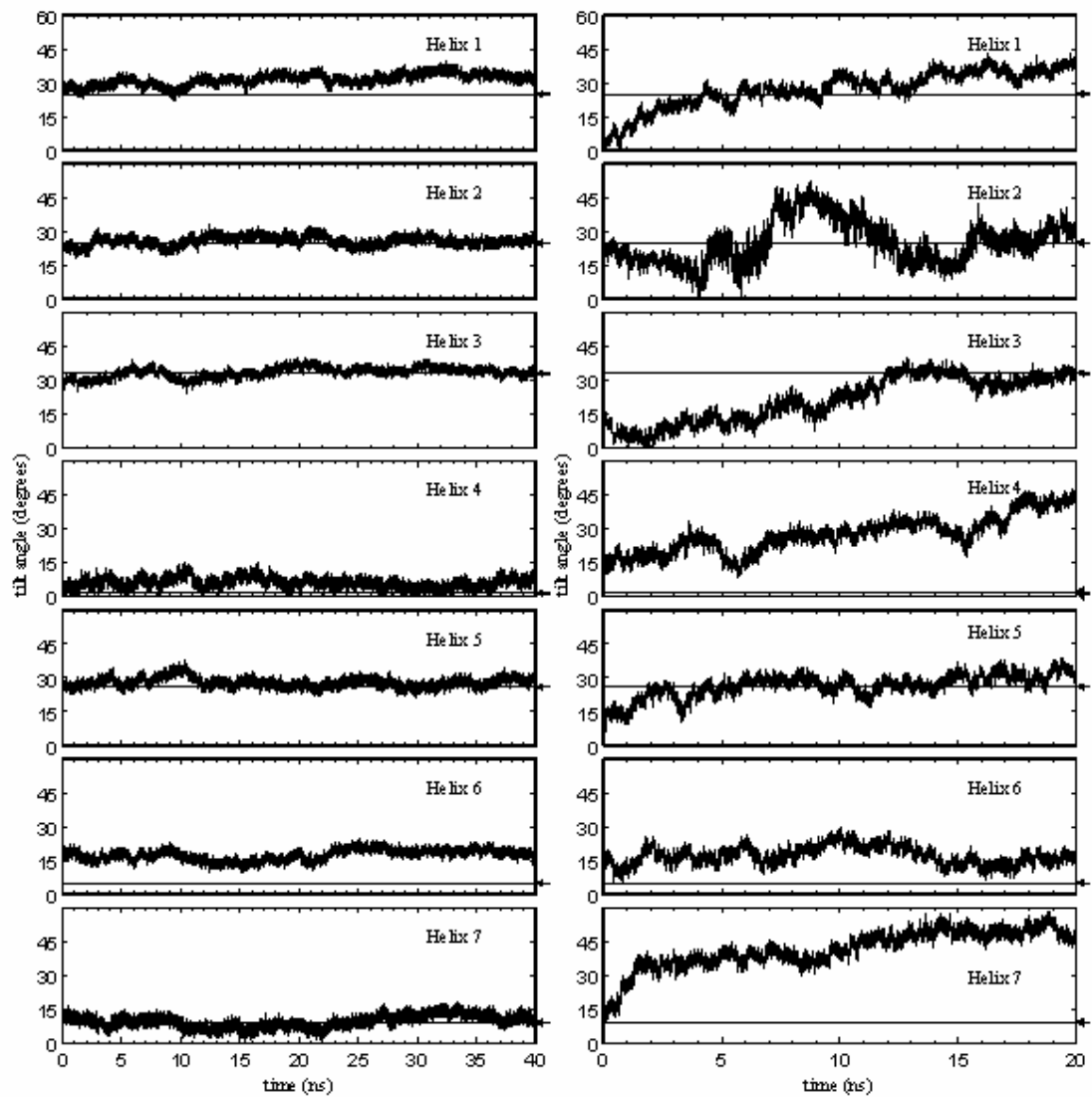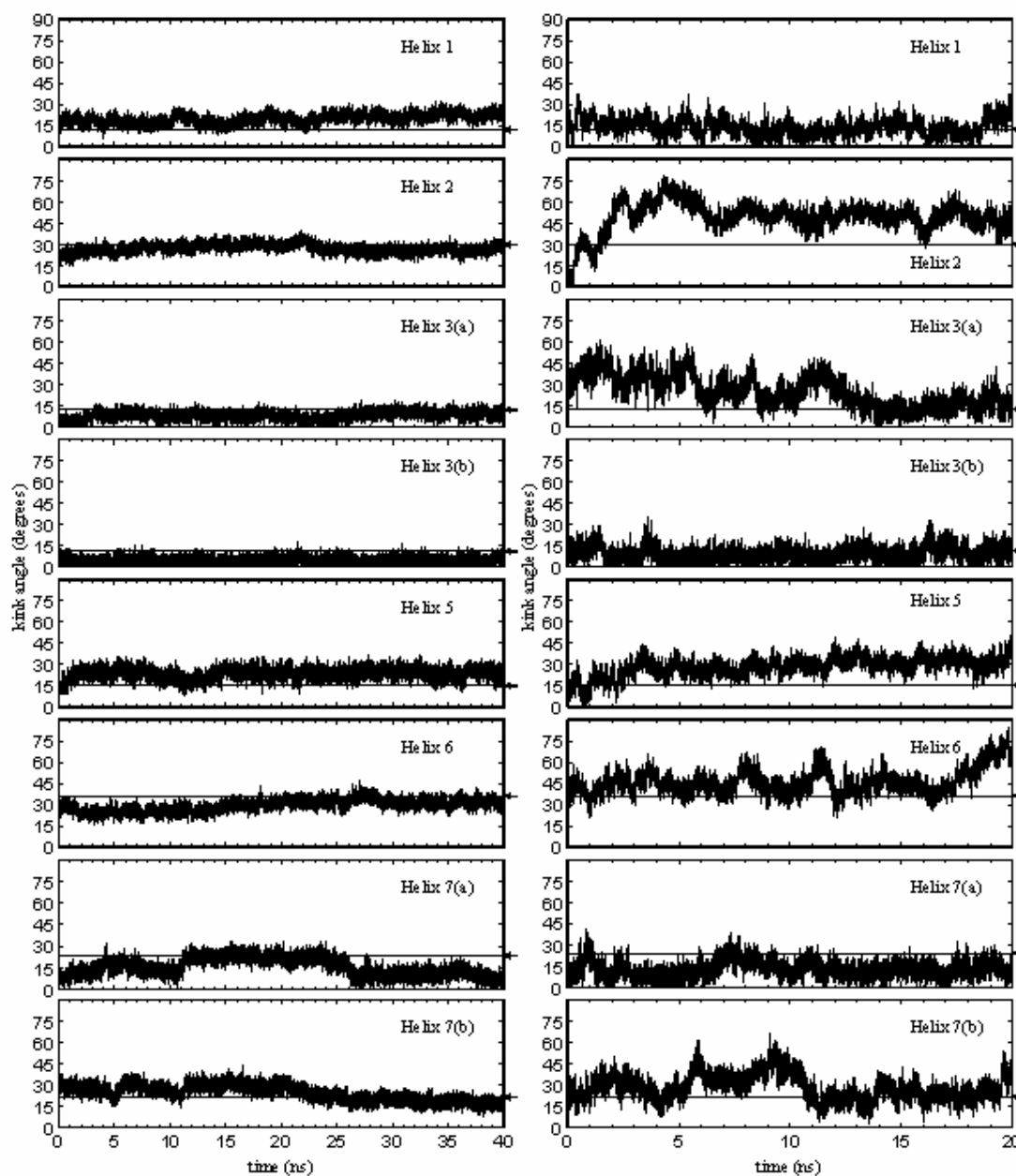
Figure 2. Helix kink angles as a function of time are shown with the intact rhodopsin helices on the left and the isolated helices on the right. Static experimentally-measured kink angles are marked by the flat lines and by the arrows on the right. Residues around which kink angles were measured are as follows: Pro 53 for Helix 1, Gly 89 for Helix 2, Gly 120 for Helix 3(a), Ser 127 for Helix 3(b), His 211 for Helix 5, Pro 267 for Helix 6, Pro 291 for Helix 7(a), and Pro 303 for Helix 7(b).
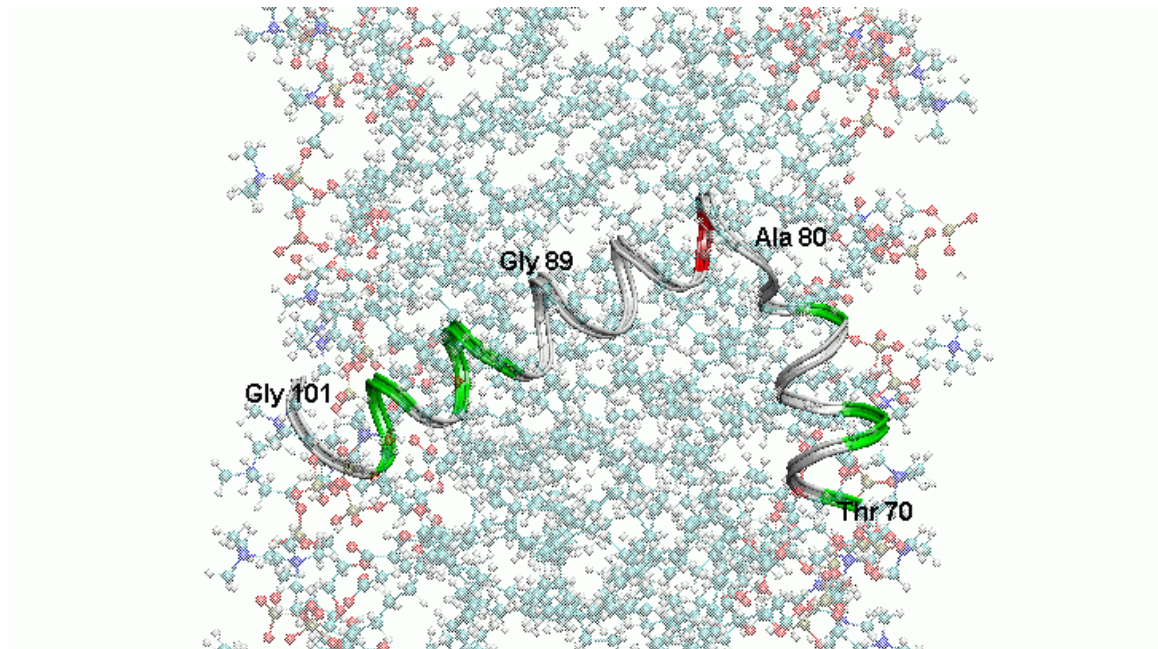
Figure 3. Snapshot from the simulation of isolated helix 2 taken at *t* = 4.5 ns showing the large kink angle centered on Ala 80. No kink forms around Gly 89 and Gly 90 as in native rhodopsin. Acidic residue Asp 83 is shown in red. Polar residues are shown in green and nonpolar residues are shown in white. The water has been omitted for clarity. The helix starts in the bottom right corner with cytoplasmic residue Thr 70 and ends on the left with extracellular residue Gly 101.
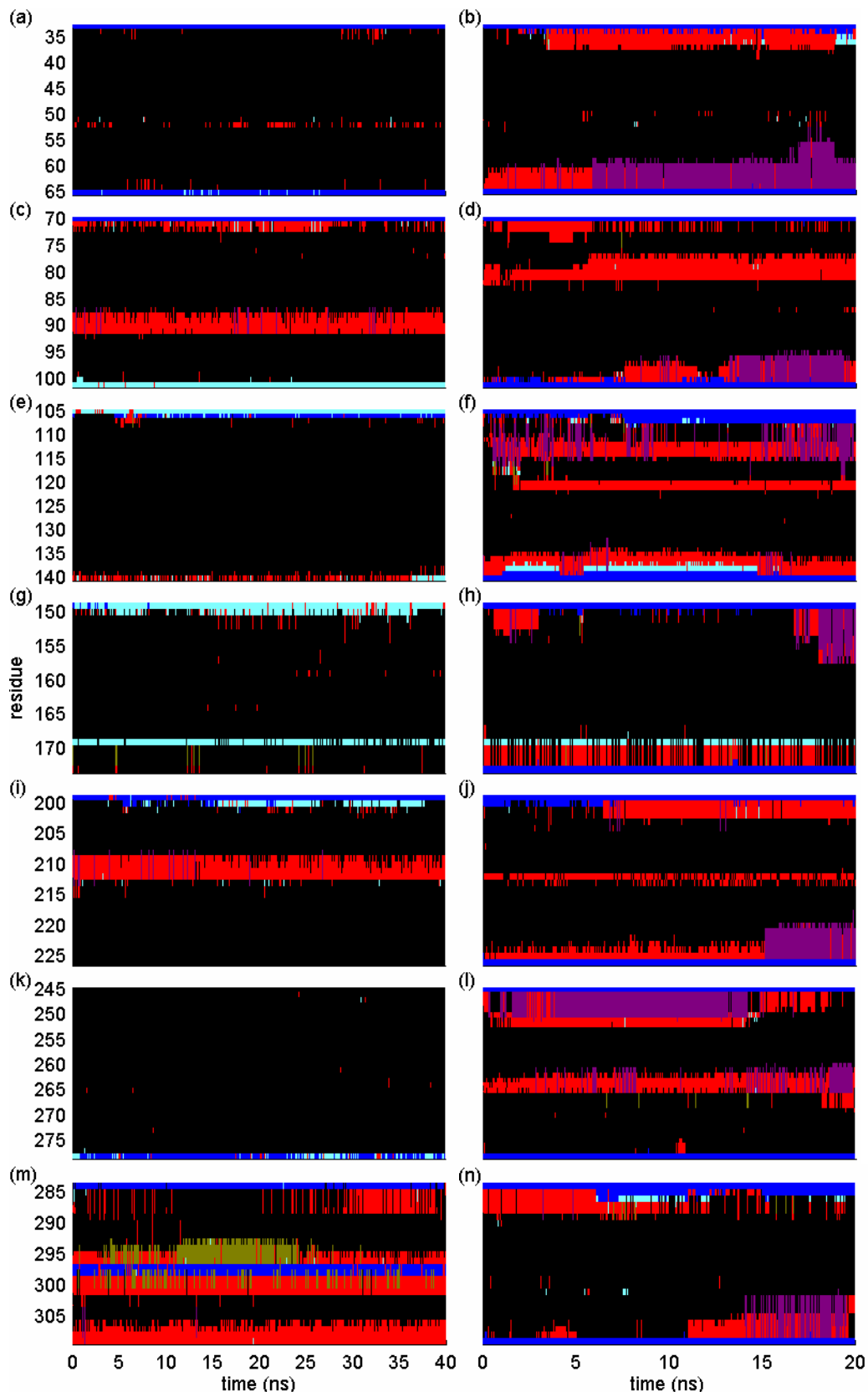
Figure 4. DSSP analysis of intact (left) and isolated (right) rhodopsin helix simulations. Helical regions are predominately characterized as α-helical (black), but exhibit a substantial number of H-bonded turn (red) regions. Unstructured (dark blue) and bend regions (cyan) are usually found at the ends of the α-helices. Regions of the isolated α-helices are often found to degenerate into more loosely coiled π-helical (purple) regions. The only substantial region of 3_{10} helix (olive) formation was observed from 11 to 24 ns in the intact rhodopsin simulation of Helix 7 near Ala 295 and Lys 296.

Chapter 4 Atomistic Simulations of Biologically Realistic Transmembrane Potential Gradients

Jonathan N. Sachs,[1] Paul S. Crozier[2] and Thomas B. Woolf[3]

[1]Department of Molecular Biophysics and Biochemistry, Yale University, New Haven, CT 06520, USA

[2]Department of Computational Materials and Molecular Biology, Sandia National Laboratories, Albuquerque, NM 87185-0310, USA

[3]Department of Physiology, The Johns Hopkins University School of Medicine, Baltimore, MD 21205, USA

Abstract

We present all-atom molecular dynamics simulations of biologically realistic transmembrane potential gradients across a DMPC bilayer. These simulations are the first to model this gradient in all-atom detail, with the field generated solely by explicit ion dynamics. Unlike traditional bilayer simulations that have one bilayer per unit cell, we simulate a 170 mV potential gradient by using a unit cell consisting of three salt-water baths separated by two bilayers, with full three-dimensional periodicity. The study shows that current computational resources are powerful enough to generate a truly electrified interface, as we show the predicted effect of the field on the overall charge distribution. Additionally, starting from Poisson's equation, we show a new derivation of the double integral equation for calculating the potential profile in systems with this type of periodicity.

Introduction

Through high-resolution structures of ion channels, we can now begin to understand and model membrane excitability on an atomic level.[1] The connection between ion channel structure and function fundamentally relies upon the transmembrane potential gradient, which drives channel gating and ion permeation[Hille, Gennis]. The transmembrane potential is generated by: 1. Charge imbalance across the bilayer due to anion and cation populations. 2. The surface, or zeta potential due to charges in the lipid headgroups. 3. The dipole potential, due to ordering of partial charges and waters within the bilayer.[Clarke] Experimental approaches give macroscopic information about these three components, via patch-clamp[Neher], electrophoretic mobility[McLaughlin] and voltage-sensitive dyes[Clarke] respectively. The microscopic functional form of the potential has been elusive. None of the available experimental techniques have the resolution necessary to elucidate the microscopic form, nor origin, of the potential profile. Thus, theoretical and computational models that can reveal such detailed descriptions are desired.

All-atom molecular dynamics (MD) simulations have been used successfully to study details of interactions between ions and ion channels[2-4] and between ions and bilayers.[5-9] But because of limitations in the time- and length-scales accessible to all-atom simulations, MD has not been used to explicitly model the transmembrane potential gradient. Biologically relevant potential gradients are on the order of 100 mV, corresponding to a small asymmetric build-up of ions in the interfacial regions of the two monolayer leaflets of a lipid bilayer (on the order of 1 excess ion/10^4 Å^2 of bilayer).[11] An all-atom representation of this ion:lipid ratio requires on the order of 10^5 atoms, historically too many. This limitation led to the development of implicit representations of both the transmembrane potential and the membrane itself, which have reduced number of atoms. In one important example, the Poisson-Boltzmann equation was modified to include the effect of a potential and used to calculate the charge distribution in the continuum and the electric field in the pore of an ion channel.[11,12] Another approach that avoids the need for huge bilayers has been to include an additional term in the MD force function, to account for the potential.[13,14] As with the continuum methods, this approach has relied upon a dielectric description of membrane ($\varepsilon = 2$) and water ($\varepsilon = 80$) in setting the position-dependent strength of the applied field.

In addition to the problem of limited simulation size, the need for periodic boundary conditions is a major hurdle to all-atom simulations of the transmembrane potential. Because simulations that employ electrostatic cut-offs suffer from well-known artifacts,[15-17] most modern simulations apply the Ewald summation technique for calculating long-range electrostatic interactions.[18] One requirement of the traditional Ewald sum is that the system must be periodically replicated in all three dimensions, including the one normal to the bilayer and parallel to the potential gradient. In order to establish and equilibrate a potential gradient, the salt-water baths on opposite sides of the bilayer (carrying the charge imbalance) cannot be connected periodically, as is the case in the traditional unit cell used for all-atom bilayer simulations. A similar problem has been addressed in simulations of salt-water embedded between oppositely charged electrodes.[19-23] An Ewald sum that eliminates the need for periodicity in one dimension

can be used for long-range electrostatic calculations,[24-26] but the computational implementation is prohibitively slow.[21,27,28] An alternative is to modify the three dimensional Ewald sum and diminish the periodic interactions between the two salt-water baths by separating them with vacuum regions.[22] This method has been used recently in models of bilayer concentration gradients[29] and in an all-atom ion channel simulation.[30]

A straightforward solution to the periodicity problem is to simulate more than one bilayer per unit cell, but until now this has been considered too computationally expensive. Here, we take this approach, which allows for full three-dimensional periodicity and an all-atom representation of the transmembrane potential with no continuum approximations. Specifically, we simulate a system with three salt-water baths separated by two bilayers. The central salt-water bath carries a net charge of +1 e, while the two outer water baths, connected periodically, each carry, on average, a net charge of –0.5 e, hence eliminating the periodicity problem. We show a 170 mV potential gradient that, on a 10 ns timescale, affects the charge distribution in the entire system. A simulation with no potential gradient is also presented as a baseline for comparison. This approach is consistent with a recent simulation of a model membrane.[10] We also derive a double integral equation from Poisson's equation for calculating the potential profile in systems with this type of periodicity.

Methods

Two double-bilayer systems were built using the CHARMM molecular mechanics package,[31] one with a charge imbalance due to excess ions (electrified) and one with no such imbalance (neutral). Details of the ion distributions are given in Table 1, and Fig. 1 shows a snapshot from the electrified simulation. Proceeding from the left-most point, there is an outer salt-water bath (-0.5 e), a bilayer (outer and then inner monolayer), a central salt-water bath (+1.0 e), a second bilayer (inner then outer monolayer) and finally a second outer water bath (-0.5 e). The initial configuration had 1 excess Na^+ in the central salt-water bath, and 1 excess Cl^- in the right-most salt-water bath. The system was built to optimize the trade-off between system size and a realistic potential drop. The voltage drop was predicted based upon the relation V=Q/C, where Q is the net charge per unit area and C is the capacitance, taken as 1 $\mu F/cm^2$, a common value used for lipid membranes.[11] The system consists of a total of 512 lipids, each of 4 monolayers having 128 lipids. Given the experimentally determined[32] area per lipid of 59.7 $Å^2$, the charge imbalance of +0.5 e/bilayer was predicted to produce a potential gradient of approximately 210 mV. Based on previous simulations[5,9] the length of the salt-water baths was set greater than the expected extent of salt-induced water ordering in the bilayer-electrolyte interface. The final dimensions were 87 x 87 x 120 Å. Na^+ and Cl^- ions were added at random locations, each replacing a water molecule, to a final concentration of 1 M. This relatively high salt concentration was chosen to maximize the sampling of the ions as has been done previously.[5,9]

We performed all-atom molecular dynamics simulations of the constructed ensembles using the CHARMM22 force field[33-34] in the 2003 version of the Large-scale Atomic/Molecular Massively Parallel Simulator (LAMMPS), which is distributed freely

as open-source software under the GNU Public License.[35-37] Bonds involving hydrogen atoms were held rigid using the SHAKE algorithm to enable a 2 femtosecond time step. The TIP3P waters were also held rigid by SHAKE. Each system was simulated at constant lipid bilayer surface area, but the simulation cell length in the z-direction was allowed to fluctuate in order to maintain isobaric conditions. A Nosé-Hoover thermostat/barostat was used to hold the simulations near 298 K and 1 atm. The z-direction box length stayed near 120 Å, with minor fluctuations, for both the neutral and the electrified system simulations.

Long-range electrostatics were computed using the particle-particle/particle-mesh (P^3M) method, which is very similar to the commonly-used particle mesh Ewald (PME) method, and has been shown to be slightly more efficient than PME.[38] We used a real-space cutoff of 10 Å, with a real-space/reciprocal-space partitioning parameter chosen for optimal speed given a desired level of accuracy.[39] The van der Waals (vdW) interactions were smoothly switched to zero between 8 and 10 Å.

Simulation of the neutral system was performed at Sandia National Laboratories on the large-scale Computational Plant (Cplant) cluster.[40] Each Cplant node is a 466 MHz 21264 (EV6) microprocessor. We were able to achieve a speed of approximately 0.3 nanoseconds of simulated time per day of compute time running in parallel on 64 processors of Cplant. The 5-ns, 2.5 million time step simulation required 18 CPU days, scattered across a month of real time, including down time. Simulation of the electrified system was performed on Sandia's Institutional Computing Cluster (ICC). Each of the ICC nodes is a dual 3.06 GHz Xenon processor. We reached a simulation speed of 0.6 nanoseconds/day running in parallel on 20 of the dual processor ICC nodes. The 10-ns, 5 million time step simulation also required 18 CPU days during a month of real time.

We now derive a new form of Poisson's equation for calculating the electrostatic potential profile in our system with its unique boundary conditions. Taking Poisson's equation,

$$\frac{d^2\phi}{dz^2} = -\frac{1}{\varepsilon_o}\sum_i q_i \rho_i(z), \tag{1}$$

where ϕ is the potential, ε_o is the permittivity constant, q_i is the charge on atom i, ρ_i is the density of atoms of type i, and z is the direction perpendicular to the membrane, we have a relationship between the equilibrium charge distribution and the potential field. Poisson's equation can be integrated twice, and the proper boundary conditions applied, in order to produce an equation that yields the potential profile as a function of z. After integrating twice, we have

$$\phi(z) = -\frac{1}{\varepsilon_o}\sum_i q_i \int_0^z \int_0^s \rho_i(u)du\,ds + C_1 z + C_2, \tag{2}$$

where u and s are dummy variables, C_1 and C_2 are constants of integration. We switch the order of integration to get

$$\phi(z) = -\frac{1}{\varepsilon_o}\sum_i q_i \int_0^z \int_u^z \rho_i(u)ds\,du + C_1 z + C_2. \tag{3}$$

Now, performing the inner integral, we obtain

$$\phi(z) = -\frac{1}{\varepsilon_o}\sum_i q_i \int_0^z (z-u)\rho_i(u)du + C_1 z + C_2. \tag{4}$$

Since all simulations in this work have been done with periodic boundary conditions (PBC), we apply PBC, requiring that $\phi(0) = \phi(L)$, where L is the simulation box length in the z-direction. In addition, we arbitrarily choose $z = 0$ as the reference point and set $\phi(0) = 0$. Applying these conditions, C_2 becomes 0, and

$$C_1 = \frac{1}{\varepsilon_o L} \sum_i q_i \int_0^L (L-u)\rho_i(u)du \ . \tag{5}$$

Finally, we have

$$\phi(z) = -\frac{1}{\varepsilon_o} \sum_i q_i \left[\int_0^z (z-u)\rho_i(u)du - \frac{z}{L}\int_0^L (L-u)\rho_i(u)du \right]. \tag{6}$$

In practice, atomic charges are accumulated in narrow bins ($\Delta z \sim 0.1$ Å) positioned along the z-axis, perpendicular to the membrane surface. Snapshots of the dynamic system taken at 1 ps intervals provide a time-averaged net charge for each bin. A potential profile that is representative of the equilibrium state of the given system is then obtained by summing up the bins using Eq. 6.

Results & Discussion

Fig. 2 demonstrates the basic aim of this study: electrified bilayers can now be simulated with the multi-layer method. The electrostatic potential profiles from both the neutral and electrified bilayer simulations, as calculated from Eq. 6, are given in Fig. 2a. The most important feature is a potential gradient of 170 mV across both of the bilayers in the electrified simulation. Additionally, the shape of the profile in the electrified simulation is consistently different when comparing the outer and inner monolayers within each bilayer, reflecting their exposure to opposite ends of the electrical gradient. The significant changes in the center of the bilayers reflect the impact of the electrical gradient on the dipolar orientations of the hydrocarbon chains, and hence the dipole potential as described above. These differences are diminished in the neutral case, as would be expected. Comparing the two simulations, it is not until deep within the lipid headgroup region (at approximately the level of the carbonyl groups) that the two profiles begin to diverge. The two potential profiles are identical in both of the outer salt-water baths, and level off in all three of the salt-water baths, showing that the simulation dimensions are large enough to accommodate the potential drop and charge screening.

The equilibration of the potential profile is of central concern in evaluating this multi-layer method for simulating transmembrane potential gradients. Fig. 2 suggests that the relatively short timescale of these simulations is sufficient for the equilibration of the potential profile. In both simulations the profiles across the two bilayers are nearly identical, though there are some subtle variations deep within the hydrocarbon regions. To minimize the size of the simulations and still achieve a potential gradient relevant to real membranes, the electrified system has the minimum number of excess charges (1 Cl⁻ shared between each of the outer salt-water baths): only one of the two outer baths started with an excess Cl⁻ in the initial configuration. Fig. 2a shows that this single excess Cl⁻ samples both periodically-connected outer water-baths sufficiently. The overall shape of the potential profiles is consistent with previously published results.[41] Fig. 2b shows the

temporal build-up of the potential profile from the electrified simulation, starting from the initial configuration and proceeding through the first 10 ps, 1 ns and the full 10 ns. Data has been averaged over the two bilayers in order to take full advantage of the doubled sampling available from this system configuration. The overall shape of the potential profile equilibrates rapidly (on the order of several ps, only a few thousand timesteps). Within the lipid region, the equilibration period is a bit longer, but is still only on the order of nanoseconds. The potential drop of 170 mV is somewhat lower than that predicted (see Methods), but we believe this difference to be a minor one that partially reflects the uncertainty in the simulated membrane capacitance. Additionally, the potential profile for the neutral simulation shows a small non-zero gradient, which most likely reflects finite size-effects, and will be addressed in future reports.

By integrating the total charge density, Fig. 3 shows the asymmetric build-up of charge in the interfacial region of the outer and inner monolayers. As would be predicted based upon the direction of the electric field, there is an excess of negative charge at the outer monolayer and an excess of positive charge at the inner monolayer, inside of the two carbonyl distributions (18 Å $< z <$ 46 Å; note the bilayer center is at $z =$ 30 Å). The two curves are nearly identical in the salt-water baths, but the electrified curve becomes more negative at $z \approx$ 18 Å and then more positive at $z \approx$ 40 Å. The locations of these two transitions are thus shifted by approximately 2 Å, which may reflect a difference in penetration depth of the Cl^- and Na^+.[5-7,9] In addition to affecting the overall charge distribution, the electric field also affects the distributions of individual lipid chemical groups (not shown). Specifically, in the electrified simulation the inner leaflet distributions tend to be sharper and narrower than those of the outer leaflets. This phenomenon is not observed in the neutral case, in which the distributions are symmetric in all monolayer leaflets. Such differences in the molecular distributions at the outer and inner monolayers, in addition to those shown in Fig. 3, confirm that the statistical sampling of the charge imbalance is enough to impact the overall equilibrated charge distribution.

In conclusion, we have shown that current computational resources are sufficient for simulating an explicit and biologically relevant transmembrane potential. Specifically, simulations with a central unit cell consisting of two bilayers separating three salt-water baths avoid the periodicity problem. While these simulations are by necessity quite large, we show here that they should now be considered an option, and may be used to complement and evaluate more tractable approaches including continuum models and applied electric fields. We have shown that even on a short time-scale (10 ns in this case) the dynamic sampling of the charge imbalance clearly affects the overall charge distribution, consistent with the direction of the electric field. Additionally, we have presented a new derivation of the double integral equation for this periodic geometry that should be used in future applications of this method. Our method may be used in future studies to evaluate assumptions made in the more computationally tractable continuum approaches described above. Additionally, all-atom simulations such as those presented here achieve a level of detail which can in the future be used to evaluate the specific role of water and salt ions in establishing the electric field, and to parse local and global effects on the lipids. Ongoing simulations will address the effect of the potential gradient on the dynamics of lipid components, specifically the headgroup and chain order parameters.

Acknowledgements

References

[1] Y. Zhou and R. MacKinnon, Biochem. 43, 4978 (2004).

[2] J. D. Faraldo-Gomez and B. Roux, J. Mol. Bio. 339, 981(2004).

[3] S. Berneche and B. Roux, Nature 414 73 (2001).

[4] I. H. Shrivastava and M. S. P. Sansom, Eur. Biophys. J. Biophys. Lett. 31, 207 (2002).

[5] J. N. Sachs and T. B. Woolf, J. Amer. Chem. Soc. 125, 8742 (2003).

[6] R. A. Bockmann, A. Hac, T. Heimburg and H. Grubmuller, Biophys J. 85, 1647 (2003).

[7] S. A. Pandit, D. Bostick and M. L. Berkowitz, Biophys J. 84, 3742 (2003).

[8] P. Mukhopadhyay, L. Monticelli L, D. P. Tieleman, Biophys J. 86, 1601 (2004).

[9] J. N. Sachs, H. Nanda, H. I. Petrache and T. B. Woolf, Biophys J. 86, 3772 (2004).

[10] J. Dzubiella, R. J. Allen and J. P. Hansen, J. Chem. Phys. 120, 5001 (2004).

[11] B. Roux, Biophys. J. 73, 2980 (1997).

[12] B. Roux, Biophys. J. 77, 139 (1999).

[13] D. P. Tieleman, H. J. C. Berendsen and M. S. P. Sansom, Biophys. J. 80, 331 (2001).

[14] A. Suenaga, Y. Komeji, M. Uebayasi, T. Meguro, M. Saito and I. Yamato, Biosci. Rep. 18, 39 (1998).

[15] G. S. Del Buono, T. S. Cohen and P. J. Rossky, J. Mol. Liq. 60, 221 (1994).

[16] J. E. Roberts and J. J. Schnitker, Chem. Phys. 102, 450 (1995).

[17] S. G. Kalko, G. Sese, and J. A. Padro, J. Chem. Phys. 104, 9578 (1996).

[18] C. Sagui and T. A. Darden, Annu. Rev. Biophys. Biomol. Struc. 28, 155 (1999).

[19] L. Perera, U. Essmann, and M. L. Berkowitz, Langmuir 12, 2625 (1996).

[20] J. N. Glosli and M. R. Philpott, Electrochim. Acta 41, 2145 (1996).

[21] E. Spohr, J. Chem. Phys. 107, 6342 (1997).

[22] I. C. Yeh and M. L. Berkowitz, J. Chem. Phys. 111, 3155 (1999).

[23]P. S. Crozier, R. L. Rowley, E. Spohr, and D. J. Henderson, Chem. Phys 112, 9253 (2000).

[24]D. E. Parry, Surf. Sci 49, 433 (1975).

[25]D. M. Heyes, M. Barber and J. H. R. Clarke, J. Chem. Soc., Faraday Trans. II 73, 1485 (1977).

[26]S. W. de Leeuw and J. W. Perram, Mol. Phys. 37, 1313 (1979).

[27]S. Y. Liem and J. H. R. Clarke, Mol. Phys. 92, 19 (1997).

[28]A. H. Widmann and D. B. Adolf, Comput. Phys. Commun. 107, 167 (1997).

[29]J. N. Sachs, H. I. Petrache, D. M. Zuckerman and T. B. Woolf, J.Chem. Phys. 118, 1957 (2003).

[30]D. Bostick and M. L. Berkowitz, Biophys. J. 85, 97 (2003).

[31] B. R. Brooks, R. E. Bruccoleri, B. D. Olafson, D. J. States, S. Swaminathan and M. Karplus, J. Comp. Chem. 4**,** 187 (1983).

[32]H. I. Petrache, S. Tristram-Nagle and J. F. Nagle, Chem. Phys. Lip 95, 83 (1998).

[33]http://www.pharmacy.umaryland.edu/faculty/amackere/force_fields.htm/par_all22_prot.inp

[34]A. D. MacKerell, Jr., D. Bashford, M. Bellott, R. L. Dunbrack, Jr., J. D. Evanseck, M. J. Field, S. Fischer, J. Gao, H. Guo, S. Ha, D. Joseph-McCarthy, L. Kuchnir, K. Kuczera, F. T. K. Lau, C. Mattos, S. Michnick, T. Ngo, D. T. Nguyen, B. Prodhom, W. E. Reiher, III, B. Roux, M. Schlenkrich, J. C. Smith, R. Stote, J. Straub, M. Watanabe, J. Wiorkiewicz-Kuczera, D. Yin and M. Karplus, J. Phys. Chem. B, 102, 3586 (1998).

[35]http://www.cs.sandia.gov/~sjplimp/lammps.html

[36]S. J. Plimpton, J. Comput. Phys., 117, 1 (1995).

[37]S. J. Plimpton, R. Pollock and M. Stevens, *Particle-Mesh Ewald and rRESPA for Parallel Molecular Dynamics Simulations,* in Proc of the Eighth SIAM Conference on Parallel Processing for Scientific Computing, Minneapolis, MN, March 1997.

[38]M. Deserno and C. J. Holm, J. Chem. Phys., 109, 7678 (1998).

[39]M. Deserno and C. J. Holm, J. Chem. Phys., 109, 7694 (1998).

[40]http://www.cs.sandia.gov/cplant/

[41]L. Saiz and M. L. Klein, J. Chem. Phys 116, 3052 (2002).

B. Hille, *Ionic Channels of Excitable Membranes* (Sinauer Associates, Sunderalnd, 1992).

R.B. Gennis, *Biomembranes: molecular structure and function* (Springer-Verlag, 1989).

R. J. Clarke, Adv. Coll. Int. Sci. 89-90, 263 (2001).

McLaughlin, S. Annu. Rev. Biophys. Biophys. Chem. 18, 113 (1989).

E. Neher, B. Sakmann. Nature. 260, 799 (1976).

Table 1. Number of ions in the starting configuration for each of the three salt-water baths shown in Fig. 1. In each case the concentration is 1 M, with the central region having 1 excess Na^+ and each of the two periodically connected outer regions having 0.5 excess Cl^- ions on average.

Simulation	Bath 1	Bath 2	Bath 3
Neutral	60 Na^+, 60 Cl^-	120 Na^+, 120 Cl^-	60 Na^+, 60 Cl^-
Electrified	60 Na^+, 60 Cl^-	121 Na^+, 120 Cl^-	60 Na^+, 61 Cl^-

FIGURE CAPTIONS

FIG. 1. Snapshot from the 170 mV simulation showing the three regions of salt-water separated by the two bilayers. There is an excess of 1 Na$^+$ in the central bath and 1 Cl$^-$ in the two outer baths combined. The ions are represented as spheres.

FIG. 2. Transmembrane potential profiles. (a) The profile from the neutral (long-dashed line) and 170 mV simulations (solid line) across the entire 120 Å system shown in Fig.1 (0 Å the left-most point, 120 Å the right-most point). Vertical arrow highlights the difference in potential gradient between the two simulations. (b) Temporal build-up of the equilibrated potential profile. Symmetrized half-cell profiles from the 170 mV simulation extracted from the first 1 ps (dashed), 10 ps (dot-dashed), 1 ns (long dashed) and 10 ns (solid). Arbitrarily scaled density profiles for the lipid phosphate (dotted) and carbonyl groups (dot-dashed) from the electrified simulation are given at the bottom of both plots for spatial reference.

FIG 3. Single integral, σ, of the symmetrized charge density from the neutral (long-dashed line) and 170 mV (solid line) simulations, showing the build-up of negative charge on the outer-most monolayer leaflets ($z < 30$ Å), and positive charge on the innermost leaflets ($z > 30$ Å) as predicted. Arrows indicate the peaks in the phosphate distributions given in Fig. 2.
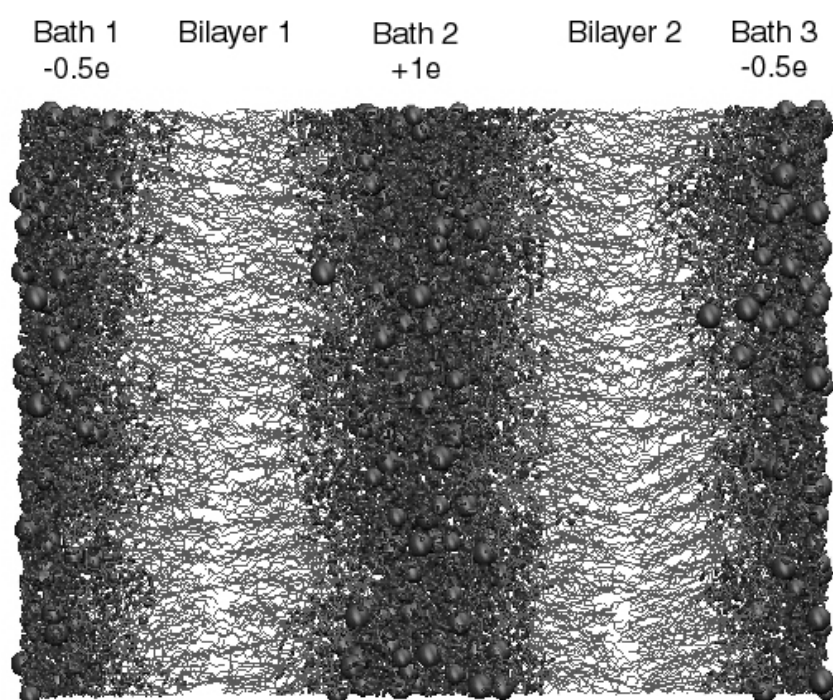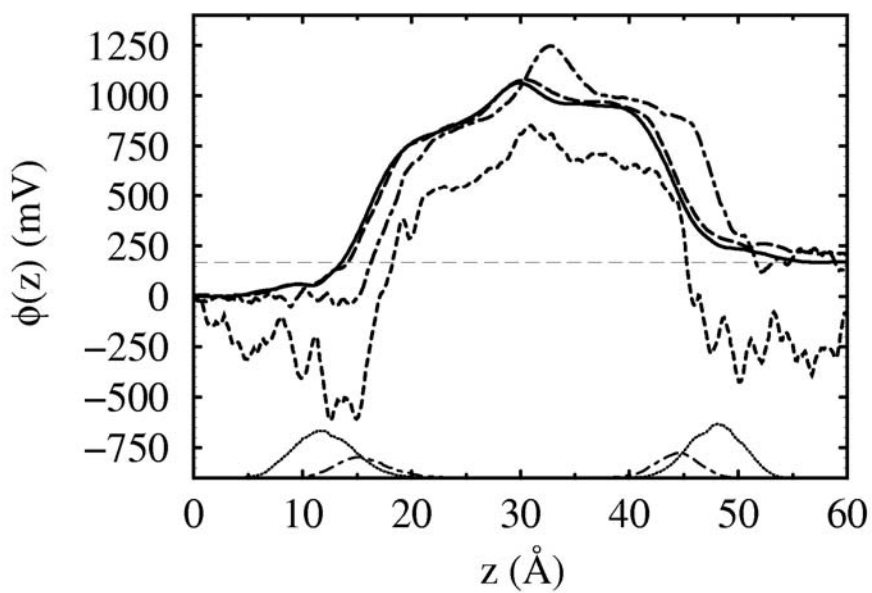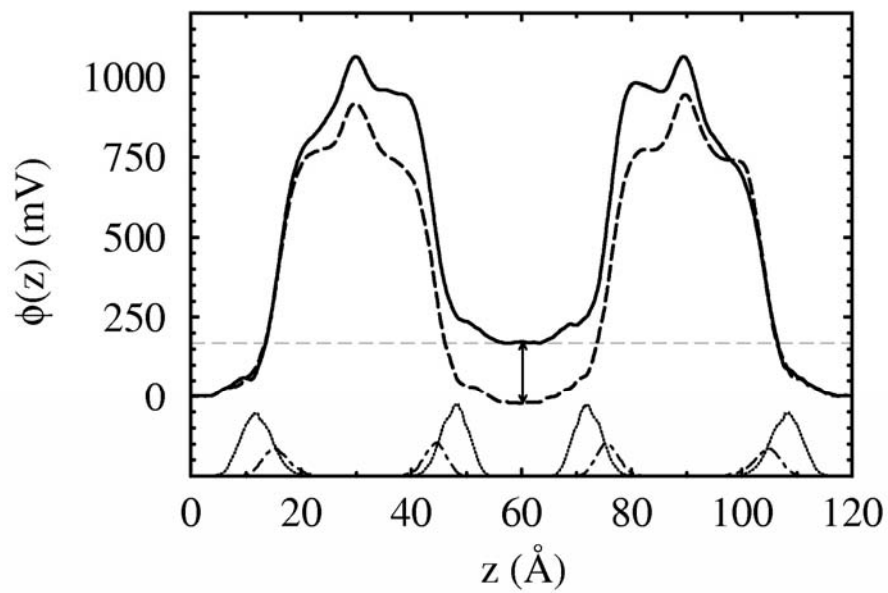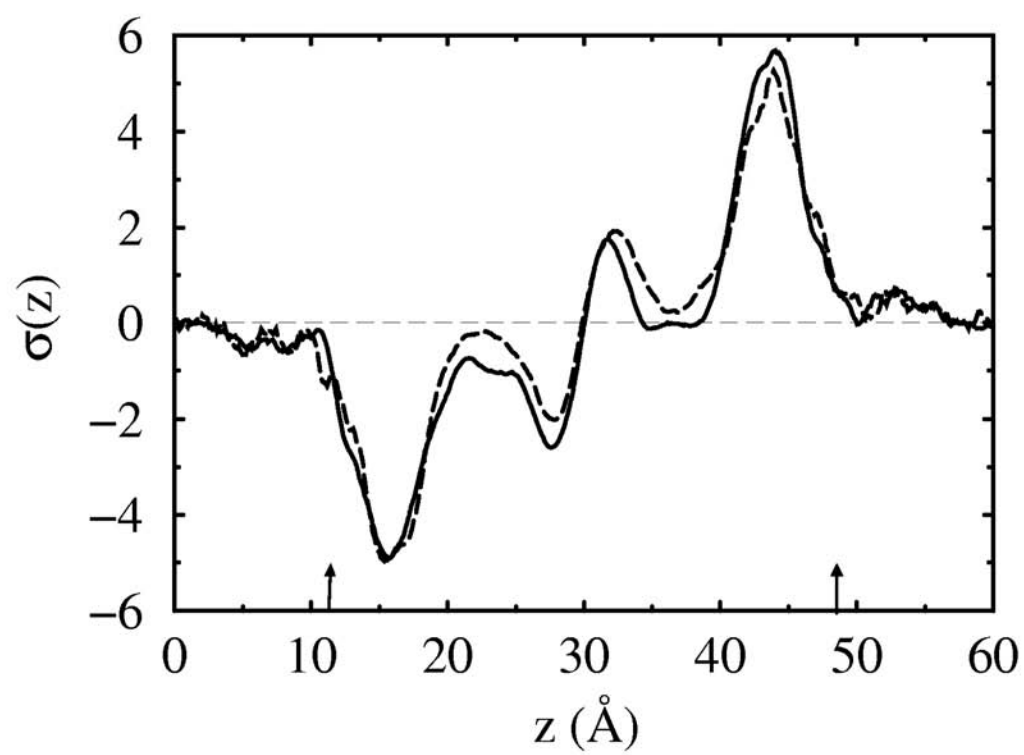
FIG. 1.

Bath 1   Bilayer 1   Bath 2   Bilayer 2   Bath 3
-0.5e   +1e   -0.5e

FIG. 2a & 2b.

FIG. 3.

Distribution:

2	MS 0123	Donna Chavez, 1011, LDRD
1	MS 0885	Grant Heffelfinger, 1802
1	MS 1110	Paul Crozier, 9235
1	MS 1110	John Aidun, 9235
1	MS 1411	Eliot Fang, 1834
3	MS 1411	Mark Stevens, 1834
1	MS 9951	Malin Young, 8141
1	MS 9951	Joe Schoeniger, 8141
2	MS 9018	Central Technical Files
1	MS 0899	Technical Library